J. Fluid Mech. (1992), *vol.* 243, *pp.* 73–102
Printed in Great Britain

On the structure of cellular solutions in Rayleigh–Bénard–Marangoni flows in small-aspect-ratio containers

By HENK A. DIJKSTRA†
Mathematical Sciences Institute, Cornell University, Ithaca, NY 14853, USA

(Received 16 August 1990 and in revised form 14 February 1992)

Multiple steady flow patterns occur in surface-tension/buoyancy-driven convection in a liquid layer heated from below (Rayleigh–Bénard–Marangoni flows). Techniques of numerical bifurcation theory are used to study the multiplicity and stability of two-dimensional steady flow patterns (rolls) in rectangular small-aspect-ratio containers as the aspect ratio is varied. For pure Marangoni flows at moderate Biot and Prandtl number, the transitions occurring when paths of codimension 1 singularities intersect determine to a large extent the multiplicity of stable patterns. These transitions also lead, for example, to Hopf bifurcations and stable periodic flows for a small range in aspect ratio. The influence of the type of lateral walls on the multiplicity of steady states is considered. 'No-slip' lateral walls lead to hysteresis effects and typically restrict the number of stable flow patterns (with respect to 'slippery' sidewalls) through the occurrence of saddle node bifurcations. In this way 'no-slip' sidewalls induce a selection of certain patterns, which typically have the largest Nusselt number, through secondary bifurcation.

1. Introduction

Variations in surface tension along a gas–liquid interface induce a shear stress on the interface. Therefore, if the bulk liquid is viscous, surface tension gradients induce bulk liquid motion, usually referred to as Marangoni convection. Since the surface tension depends on temperature and composition of the fluids at the interface, practically everywhere where gas–liquid interfaces are in the picture, Marangoni effects become visible. Strong wine creeps up the wall of a glass (the 'wine glass' effect, Thomson 1855), fast movements occur near the wick of a burning candle and small surface-crawling insects can be seen moving rapidly to safety to waterplants on the back of a film drawn by Marangoni convection once the water is suddenly polluted by surface active components.

Marangoni flows can be classified into two types: macro-scale flows and micro-scale flows (Berg 1972). This classification does not refer to the ultimate form of the convection but to its origin. Macro-scale convection is brought about by macroscopic scale asymmetry, e.g. by geometric asymmetry of the bulk phases about the interface (as in the 'wine glass' effect) or by an asymmetry in boundary conditions. An example of the latter is the thermocapillary convection in a differentially heated cavity. Micro-scale convection is triggered by an instability. This Marangoni instability was recognized by Block (1956) and Pearson (1958), to be a cause of

† Present address: Institute of Meteorology and Oceanography, University of Utrecht, Princetonplein 5, 3584 CC Utrecht, The Netherlands.

cellular convection developing in a motionless liquid layer heated from below. The critical conditions for the onset of this instability are formulated as the value of a dimensionless Marangoni number Ma, a ratio of the interfacial driving force and dissipative forces. The physical mechanism of this instability is well known (Davis 1987) and the instability is also known to be the predominant factor (Koschmieder 1974) of the formation of hexagonal cells observed by Bénard in the early 1900s.

Surface-tension-driven flows are of importance in many sections of the process industry. A few examples are considered here. In chemical engineering, the magnitude of the interface between different phases and the consequent rate of mass transfer is a high-valued design criterion. The Marangoni effect can improve or make worse the expected rate of mass transfer dramatically (Zuiderweg & Harmens 1958; Patberg *et al.* 1983). Also the influence of Marangoni convection is spectacular in the formation of holes in the compact-disk technology. Here, by lasers, very small spots on thin metal layers, spread over a polymer substrate, are heated up above the melting point of the metal. The resultant surface tension then becomes very low and thus the liquid metal is withdrawn from the illuminated spot. A craterlike point results. Other areas where Marangoni flows are important are the containerless processing of crystals, combustion, welding and the behaviour of thin films.

Flows originating from the Marangoni instability are also interesting from a more theoretical point of view. They can be placed within a group of other flows in which transitions are studied from simple to more complicated flows as some driving force (say measured by a dimensionless number R) is increased. The aim of these studies is to understand the development from laminar to turbulent flow. Examples are the Taylor–Couette flow and the buoyancy-induced flow in a saturated porous medium (or Newtonian liquid) heated from below (Rayleigh–Bénard flows).

These flows have been used to study a large number of nonlinear problems. Typically, a simple base flow (which is the only stable flow at small R) becomes unstable at some critical value of R. As R is increased, steady cellular patterns develop over a range of R and experiments show that some patterns seem to be more preferred than others, i.e. there is a selection of patterns through nonlinear interactions.

For Rayleigh–Bénard convection in large-aspect-ratio containers, the pattern selection process is well understood and theory and experiment are in good agreement (Cross *et al.* 1983). The situation is different for small-aspect-ratio containers, where both theoretical and experimental work is scarce. Here, changes in the flow pattern are highly restricted by the presence of the lateral walls. The case is interesting, however, because the dynamics is governed by the interaction of a few modes (the number depending on the distance from onset) and a link with the behaviour of dynamical systems of low dimensionality can be made.

In this paper the problem of pattern selection in small-aspect-ratio containers is addressed for flows driven by surface-tension gradients. Because of computational resources, we restrict ourselves to two-dimensional containers. Although Rayleigh–Bénard–Marangoni flows are basically three-dimensional, our study has physical relevance. In experiments, especially if the width of the container is small compared to its length, typically two-dimensional patterns are observed. Furthermore, two-dimensional results give insight into processes that govern convection dynamics in these confined flows and are a necessary starting point for any three-dimensional calculation. Finally, many three-dimensional flows result from instabilities of corresponding two-dimensional flows.

The dimensionless parameters characterizing the system are in this case the

stability parameter Ma, the Biot number Bi, the Prandtl number Pr and the aspect ratio A. Given any set of values of these parameters, the main question is now many realizable (i.e. stable) flow patterns do exist. Since the motionless conduction solution is a solution for all values of the parameters, the first step to answer this question is to calculate the onset conditions of convection, i.e. the critical values of Ma. Results are well known (cf. figure 2) and depend only on A and Bi.

At specific values of (A, Bi) two flow patterns (modes) have the same onset conditions. A nonlinear analysis of the possible flow patterns in the vicinity of these so-called double points gives insight into the qualitative change of the bifurcation structure in parameter space. This approach was followed by Rosenblat, Homsy & Davis (1982) for a container with 'slippery' sidewalls in the limit $Bi = 0$. Amplitude equations (cf. equations (10a, b) in the present paper) were obtained describing the mode interaction near certain double points. The local bifurcation structure was determined and it was found e.g. that Hopf bifurcations occur close to onset.

The analysis in Rosenblat *et al.* (1982) has two limitations. First, the results are only valid locally near the double point and the analysis itself does not provide the range of validity. It is therefore impossible to study the change of bifurcation structure with A (for fixed Bi and Pr) far above onset. Second, 'no-slip' lateral walls are expected to influence the dynamics and therefore the multiplicity of solutions essentially. The presence of 'no-slip' walls lowers the symmetry of the system with respect to 'slippery' walls and new features (e.g. convection below onset (Winters, Plesser & Cliffe 1988; Dijkstra & Van de Vooren 1989)) are known to occur.

Knowledge of the bifurcation structure far above onset and the influence of 'no-slip' lateral walls can only be obtained numerically. By performing these calculations using continuation methods, this study contributes to this knowledge. Continuation methods have already proved to be successful in other type of systems, e.g. the Taylor–Couette flow (Cliffe 1983) and Lapwood convection (Riley & Winters 1989).

The paper is organized as follows. In §2, the formulation of the problem is presented. Linear stability theory is reviewed briefly in §3. Numerical methods are outlined in §4 followed by §5 where a justification of the accuracy of the numerical solutions is presented. In §6, the change of bifurcation structure with A is presented for a container with 'no-slip' sidewalls and for fixed $Bi = 20$ and $Pr = 8$. The exchange mechanism at double points, the origin of Hopf bifurcations and the occurrence of hysteresis are studied in more detail. Section 7 describes the influence of the lateral walls by comparing the bifurcation structures obtained for 'slippery' sidewalls with those for 'no-slip' sidewalls. For a square container the change of bifurcation structure with the secondary parameters Bi and Pr is determined. It is shown that small Pr and small Bi promote the occurrence of multiple stable steady states.

The main result of this paper is that 'no-slip' sidewalls greatly influence the multiplicity of stable steady patterns. Typically they limit the range of existence of patterns consisting of an odd number of cells through the occurrence of saddle node bifurcations. In this way the 2-cell pattern with centre upflow is preferred (i.e. the only stable pattern) over a large area in (Ma, A) space.

2. Formulation

A two-dimensional container (figure 1) is partially filled with a Newtonian viscous liquid. Above the liquid is an ambient gas; the constant temperature of this gas far from the gas–liquid interface is T_0^*. By heating the bottom wall of the container up

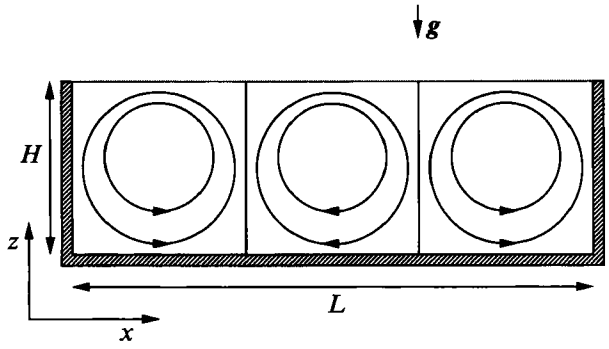

FIGURE 1. Geometrical set-up, coordinate axes are defined. Gravity points in the negative z-direction.

to a temperature T_1^*, a vertical temperature gradient is created over the layer. Heat is transferred from the liquid to the gas. The heat transfer coefficient at the interface is denoted by η. The sidewalls are assumed to be perfectly insulated. Let H and L be the height and length of the liquid layer, respectively.

The dynamic viscosity μ and thermal diffusivity κ of the liquid are constant. The density ρ of the liquid depends linearly on temperature, i.e. $\rho = \rho_0 - \alpha_1(T^* - T_0^*)$. We consider density variations only through buoyancy, whereas the liquid is assumed to be incompressible (Boussinesq approximation).

The equilibrium surface tension σ_0 of the gas–liquid interface is assumed to be large (the capillary number $C = \mu\kappa/\sigma_0 H$ is assumed to be small). In this large-surface-tension limit, the interface does not deform. Surface tension depends linearly on the interface temperature, i.e. $\sigma = \sigma_0 - \alpha_2(T^* - T_0^*)$.

We non-dimensionalize velocity, time and length by κ/H, H^2/κ and H, respectively. A non-dimensionless temperature T is given by $T^* = T(T_1^* - T_0^*) + T_0^*$. A streamfunction ψ and a vorticity ω are introduced. If u and w are the horizontal and vertical velocities then $u = \partial\psi/\partial z$, $w = -\partial\psi/\partial x$ and $\omega = \partial w/\partial x - \partial u/\partial z$.

The governing equations of the flow in the container are

$$Pr^{-1}\left(\frac{\partial\omega}{\partial t} + \frac{\partial(u\omega)}{\partial x} + \frac{\partial(w\omega)}{\partial z}\right) = \nabla^2\omega + Ra_0\frac{\partial T}{\partial x}, \tag{1a}$$

$$\omega = -\nabla^2\psi, \quad \left(\frac{\partial T}{\partial t} + \frac{\partial(uT)}{\partial x} + \frac{\partial(wT)}{\partial z}\right) = \nabla^2 T. \tag{1b, c}$$

At the bottom wall $z = 0$: $\qquad T = 1, \quad \psi = \dfrac{\partial\psi}{\partial z} = 0.$ (1d)

At the gas–liquid interface $z = 1$:

$$\psi = \omega - Ma_0\frac{\partial T}{\partial x} = \frac{\partial T}{\partial z} + Bi\,T = 0. \tag{1e}$$

At the sidewalls $x = 0, A$:

$$\psi = \frac{\partial T}{\partial x} = \epsilon\frac{\partial\psi}{\partial x} + (1-\epsilon)\frac{\partial^2\psi}{\partial x^2} = 0. \tag{1f}$$

In these equations, the dimensionless groups Pr (Prandtl), Ma_0 (Marangoni), Ra_0 (Rayleigh), A (aspect ratio) and Bi (Biot) appear which are defined as follows

$$Pr = \frac{\mu}{\rho_0 \kappa}, \quad Ra_0 = \frac{\alpha_1 g H^3 (T_1^* - T_0^*)}{\mu\kappa}, \quad Bi = \frac{\eta H}{\kappa}, \quad M\alpha_0 = \frac{\alpha_2 H (T_1^* - T_0^*)}{\mu\kappa}, \quad A = \frac{L}{H}, \tag{2}$$

where g is the acceleration due to gravity. A parameter ϵ is included in the last boundary condition of $(1f)$ to distinguish easily between the two cases of 'no-slip' ($\epsilon = 1$) and 'slippery' sidewalls ($\epsilon = 0$).

There are two types of symmetry in this problem. First, there is a $\mathbb{Z}_2$-symmetry, due to reflection with respect to the line $x = \frac{1}{2}A$, having a representation $\mathscr{R}$ given by

$$\mathscr{R}(\psi(x,z), T(x,z))^{\mathrm{T}} = (-\psi(A-x,z), T(A-x,z))^{\mathrm{T}}.$$

This symmetry is present for both values of ϵ. For $\epsilon = 0$ there are additional translational symmetries with representations $\mathscr{T}_{km}$ given by

$$\mathscr{T}_{km}(\psi(x,z), T(x,z))^{\mathrm{T}} = (\psi(x+kA/m,z), T(x+kA/m,z))^{\mathrm{T}}$$

where m is the number of cells and $k = 1, \ldots, m-1$ for $m \geqslant 2$ and $k = 1$ for $m = 1$. In this way a container with 'slippery' sidewalls can be considered as an infinite layer with artificial periodicity A. A more detailed description of symmetries in similar flows can be found in Riley & Winters (1989) and in Golubitsky & Schaeffer (1985).

Initially, the liquid is motionless ($\bar{\psi} = \bar{\omega} = 0$) and the temperature distribution is due to pure conduction. The conduction solution is given by

$$\bar{T}(z) = 1 - \frac{Bi}{Bi+1} z. \tag{3}$$

The solution $(\bar{\psi}, \bar{\omega}, \bar{T})$ defines the primary branch of steady solutions. This solution is invariant under the symmetries given by $\mathscr{R}$ and $\mathscr{T}_{km}$. Bifurcation points on this branch are referred to as primary bifurcation points. For $\epsilon = 0$ a translational symmetry is always broken in a primary bifurcation point. For $\epsilon = 1$, symmetry breaking primary bifurcations occur only when the $\mathbb{Z}_2$-symmetry is broken.

In the formulation above, the Marangoni number Ma_0 is different from that introduced by Pearson (1958), say denoted by Ma, which is commonly used in the literature. The relation between the numbers is simply $Ma = Ma_0 Bi/(Bi+1)$. In the same way, $Ra = Ra_0 Bi/(Bi+1)$. There is a good argument for using Ma_0 as the stability parameter instead of Ma. Of course, both Marangoni numbers differ only a factor $(Bi+1)/Bi$ if $Bi \neq 0$. However, if $Bi = 0$ (i.e. $\eta = 0$), the base state (3) is a constant-temperature state. For the infinite layer this state is linearly stable (Vidal & Acrivos 1956) and since Ma has a minimum at $Bi = 0$ for this case (Nield 1964) there seems to be a contradiction. However the stability is predicted correctly using Ma_0 because $Ma_0 \to \infty$ as $Bi \to 0$. The finite value of Ma at $Bi = 0$ is therefore due to the fact that Ma and Bi are not independent parameters.

3. Linear stability

The linear stability characteristics of the basic state (3) are well known. The equations $(1a–f)$ linearized around (3) describe the evolution of infinitesimally small disturbances superposed on the base state. These linearized equations admit solutions proportional to $\exp(\gamma t)$, where $\gamma = \mathrm{Re}(\gamma) + \mathrm{i}\,\mathrm{Im}(\gamma)$ is the complex growth

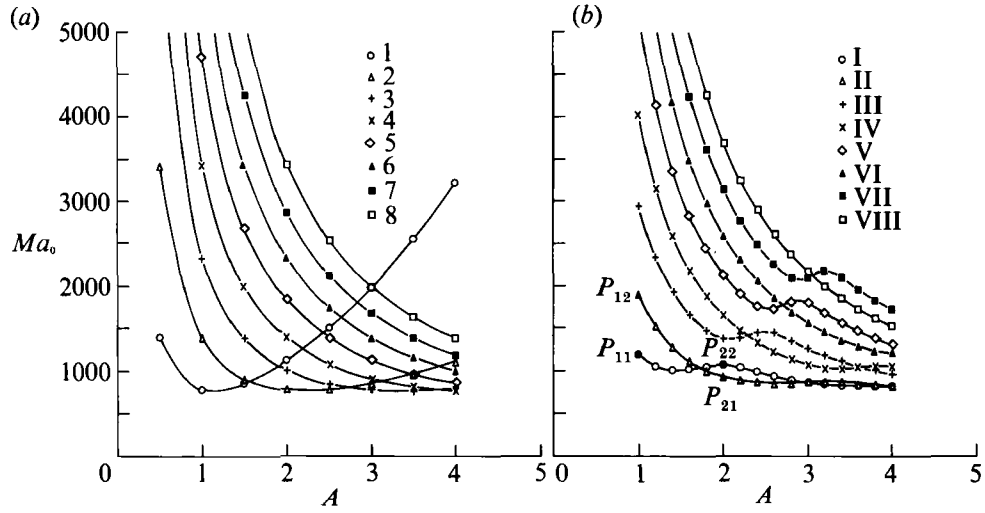

FIGURE 2. Curves of primary bifurcation points as a function of aspect ratio A, for $Bi = 20$ and (a) $\epsilon = 0$ and (b) $\epsilon = 1$.

factor. Neutral stability occurs for $\mathrm{Re}(\gamma) = 0$. It is well known that for $\epsilon = 0$ the principle of exchange of stability is valid, i.e. $\mathrm{Im}(\gamma) = 0$ at neutral stability. This is not known for the case $\epsilon = 1$. However, for the parameter region which is considered here, the numerical results in §6 show that (3) becomes unstable only through stationary modes. When $\mathrm{Im}(\gamma) = 0$, the neutral curves can be found by solving an eigenvalue problem involving the parameters Ma_0, Ra_0, Bi and A, i.e. the onset conditions are independent of Pr.

The methods of analysing this eigenvalue problem are presented elsewhere, for $\epsilon = 0$ see Nield (1964) and for $\epsilon = 1$ see Van de Vooren & Dijkstra (1989). For later reference the critical values of Ma_0 are shown as a function of A for $Ra_0 = 0$, $Bi = 20$ in figure 2(a) for $\epsilon = 0$ and in figure 2(b) for $\epsilon = 1$. If we draw a vertical line at a certain fixed A, the intersections of this line and the eigenvalue curves represent primary bifurcation points. Examples are the points P in figure 2(b) which will be referred to below. The corresponding eigenvector provides the pattern of the flow to which (locally near this bifurcation point) the motionless solution will be unstable. For $\epsilon = 0$ this pattern is constant along an eigenvalue branch (n in the figure indicates the number of cells). For $\epsilon = 1$ the pattern changes along a particular branch (Van de Vooren & Dijkstra 1989) (the roman numerals serve only to label different branches).

The value of Ma_0 at the first primary bifurcation point corresponds to onset conditions for the particular aspect ratio A. For a value of Ma_0 slightly larger than the one at onset the flow pattern with largest growth factor $\mathrm{Re}(\gamma)$ corresponds to that at onset. In this way linear theory suggests a selection of observable patterns. However, it is well known that as the amplitudes of the disturbances grow, the final steady state reached might be different than the fastest growing pattern at onset. In addition, there are certain values of A, where linear theory is ambiguous in predicting the fastest growing pattern. In both figures 2(a) and 2(b) there exist values of the aspect ratio A, so-called double points, where two patterns become unstable at the same value of Ma_0. Hence, linear theory cannot predict which finite-amplitude steady-flow patterns will eventually appear. For $\epsilon = 0$, the 1-cell and 2-cell patterns become simultaneously unstable at $A_1^0 = 1.56$; for the 2-cell and 3-cell patterns this

occurs at $A_2^0 = 2.70$. For $\epsilon = 1$, these double points occur at $A_1^1 = 1.74$ and $A_2^1 = 2.94$, respectively. In numbering the A-values of double points, the superscript refers to the value of ϵ.

4. Numerical methods

The rectangle $[0, A] \times [0, 1]$ is covered by a (non-equidistant) grid with lines parallel to the x- and z-axis. A gridpoint has subscripts (i,j), $i = 0, \ldots, n$ and $j = 0, \ldots, m$. By using the mapping

$$y = \tfrac{1}{2} + \tanh[q(\tilde{y} - \tfrac{1}{2})]/[2\tanh(\tfrac{1}{2}q)]$$

a non-equidistant grid in y is obtained from an equidistant one in $\tilde{y}$. These non-equidistant grids were employed in both the x- and z-direction; the stretching parameters q are indicated below by q_x and q_z.

The discrete version of the equations $(1a–f)$ is obtained using a finite-volume discretization method. The scheme (presented in Dijkstra 1988) is second-order accurate in space. Not only are the discrete energy equation and the discrete continuity equation satisfied exactly over the internal control volumes but also near the boundaries. The discrete equations have the symmetry properties of the continuous equations.

After discretization a system of nonlinear algebraic equations emerges which can be written as

$$\boldsymbol{\Phi}(\boldsymbol{u}, \boldsymbol{p}) = 0, \tag{4}$$

with $\boldsymbol{u} \in \mathbb{R}^d$, $d = 3(n+1)(m+1)$, $\boldsymbol{p} \in \mathbb{R}^5$ and $\boldsymbol{\Phi}: \mathbb{R}^d \times \mathbb{R}^5 \to \mathbb{R}^d$. Here $\boldsymbol{u}$ consists of values of ψ, ω and T at the gridpoints and $\boldsymbol{p}$ contains the parameters (Pr, A, Ma_0, Ra_0, Bi).

We consider system (4) as a bifurcation problem and compute branches of solutions $(\boldsymbol{u}(s), \boldsymbol{p}(s))$ of these equations, parametrized by a 'pseudo-arclength' parameter s, with continuation techniques. Here Euler–Newton continuation is used, a method well described in Keller (1977).

The investigation of the linear stability of a solution of (4) on a particular branch amounts to solving a generalized eigenvalue problem of the form

$$\boldsymbol{A}\boldsymbol{u} = \chi \boldsymbol{D}\boldsymbol{u}. \tag{5}$$

Here $\boldsymbol{A}$ is non-symmetric, banded and non-singular, while $\boldsymbol{D}$ is a singular diagonal matrix. The zeros on the diagonal of $\boldsymbol{D}$ arise through the incompressibility constraint and the Dirichlet boundary conditions.

To draw conclusions about linear stability one need not solve the eigenvalue problem completely. Only a few 'most dangerous modes', i.e. the eigenvalues closest to the imaginary axis have to be determined. The calculation of these eigenvalues for very large non-symmetric eigenvalue problems received a lot of attention recently (Goldhirsch, Orszag & Maulik 1987; Christodoulou & Scriven 1988). A relatively simple method is used here. First a mapping is defined by

$$\chi = \frac{\tau - 1}{\tau + 1}, \quad \text{for } \tau \in \mathbb{C}/\{-1\}. \tag{6}$$

The half-plane $\mathbb{C}^-$, the imaginary axis and the half-plane $\mathbb{C}^+$ are mapped onto $|\tau| < 1$, $|\tau| = 1$ and $|\tau| > 1$, respectively. The problem (5) is now reduced to the calculation of the dominant eigenvalues τ of the eigenvalue problem

$$-(\boldsymbol{A} + \boldsymbol{D})\boldsymbol{u} = \tau(\boldsymbol{A} - \boldsymbol{D})\boldsymbol{u}. \tag{7}$$

This is solved in the following way. Start with a number of vectors equal to the desired number of eigenvalues (usually 4–6). Now, because (7) contains infinite eigenvalues, components in the directions of the corresponding eigenvectors are first filtered out of the starting vectors by inverse iteration. On the remaining vectors the simultaneous iteration technique (SIT) (Steward & Jennings 1981) is applied to determine the dominant eigenvalues of (7). To obtain a matrix vector product needed during the filtering stage of the SIT, the matrix $\boldsymbol{A}-\boldsymbol{D}$ has to be decomposed. However, this decomposition can be saved throughout the SIT and therefore has to be computed only once to determine the dominant eigenvalues of (7). The residual error was determined by backsubstitution of the eigensolution into the original matrix equations (5). As stopping criterion for the SIT this error divided by the L_2-norm of the corresponding eigenvector was required to be smaller than 10^{-5}. The simultaneous iteration works well if a good approximation of the eigenvectors and eigenvalues is available. The continuation technique provides these approximations. One only has to start once with random vectors for which the algorithm does indeed take the most time.

If all eigenvalues have negative real parts, the steady state is linearly stable. If at least one eigenvalue has a positive real part, the steady state is unstable. Hopf bifurcation points (where a complex pair of eigenvalues $\sigma = \xi \pm i\tau$ crosses the imaginary axis with $\partial\xi/\partial s > 0$, where s is the arclength parameter) are detected by applying a secant algorithm to locate the point s where $\xi = 0$. Simple bifurcation points and limit points were calculated by applying a second iteration to find a zero of $\det(\boldsymbol{A})$ and $\partial Ma_0/\partial s$, respectively.

Continuation of normal limit points in a secondary parameter ζ was done using 'pseudo' arclength continuation on the extended system proposed in Moore & Spence (1980). This amounts to solving the following system of equations:

$$\boldsymbol{\Phi}(\boldsymbol{u}, \lambda, \zeta) = 0, \quad \boldsymbol{\Phi}_{\boldsymbol{u}}(\boldsymbol{u}, \lambda, \zeta)\,\boldsymbol{\phi} = 0, \tag{8a, b}$$

$$\boldsymbol{e}_k^{\mathrm{T}}\boldsymbol{\phi} = 1, \quad (\boldsymbol{u}-\boldsymbol{u}_0)^{\mathrm{T}}\dot{\boldsymbol{u}}_0 + (\boldsymbol{\phi}-\boldsymbol{\phi}_0)^{\mathrm{T}}\dot{\boldsymbol{\phi}}_0 + (\lambda-\lambda_0)\,\dot{\lambda}_0 + (\zeta-\zeta_0)\,\dot{\zeta}_0 = 0, \tag{8c, d}$$

where $\boldsymbol{\Phi}_{\boldsymbol{u}}$ is the Jacobian of (4), λ is the primary parameter (usually Ma_0), the dot indicates differentiation to the 'arclength' parameter s and the subscript 0 indicates a known solution along the branch of limit points. A starting point is provided by the solution at a specific limit point and the eigenvector corresponding to the zero eigenvalue in the corresponding stability problem. A starting tangent $(\dot{\boldsymbol{u}}, \dot{\boldsymbol{\phi}}, \dot{\lambda}, \dot{\zeta})$ is found by solving the linear system which emerges after Newton linearization of (8) with right-hand side $(\boldsymbol{0}, 0, 0, 1)$. Thereafter this tangent is normalized with respect to the L_2-norm. The particular value of k in (8c) was taken to be the absolute largest component in the starting vector $\boldsymbol{\phi}$.

The solution method of the system (8) via the Newton method and decoupling of linear systems as given by Moore & Spence (1980) was used. Basically, a modified matrix $\tilde{\boldsymbol{\Phi}}_{\boldsymbol{u}}$ (the matrix $\boldsymbol{\Phi}_{\boldsymbol{u}}$ with the kth column replaced by $\boldsymbol{\Phi}_{\lambda}$) has to be decomposed. However, although $\boldsymbol{\Phi}_{\boldsymbol{u}}$ is banded, $\tilde{\boldsymbol{\Phi}}_{\boldsymbol{u}}$ is not, and decomposing $\tilde{\boldsymbol{\Phi}}_{\boldsymbol{u}}$ would increase the computational time enormously. To avoid this, $\tilde{\boldsymbol{\Phi}}_{\boldsymbol{u}}$ was block-decomposed (taking effectively its kth row and column out, restoring the bandedness) and the remaining matrix system was solved in block form. In this way, only two decompositions of a banded matrix had to be computed per Newton step.

Continuation of $\mathbb{Z}_2$-symmetry breaking bifurcation points was done also using the extended system (8). However, now the solution $\boldsymbol{u}$ has to belong to one symmetry class, whereas the kernel $\boldsymbol{\phi}$ has to belong to the other class (Werner & Spence 1984). This was implemented by restricting the equations to the domain $[0, \frac{1}{2}A] \times [0, 1]$ and

n	m	q_x	q_z	A	Bi	ϵ	Ma_{01}	Ma_{02}
16	16	1	3	1	20	0	788.91	1438.9
32	32	1	3	1	20	0	783.01	1403.4
64	64	1	3	1	20	0	781.66	1394.8
exact							781.18	1391.9
32	16	1	3	4	20	0	811.41	825.29
64	16	1	3	4	20	0	788.91	810.95
128	16	1	3	4	20	0	783.36	807.43
exact							781.18	805.77
16	16	1	3	1	1	1	488.11	—
16	16	3	3	1	1	1	446.47	—
32	32	1	3	1	1	1	441.07	—
32	32	3	3	1	1	1	429.48	—
64	64	1	3	1	1	1	428.72	—
64	64	3	3	1	1	1	425.62	—
16	8	3	3	2	1	1	310.81	370.55
32	16	3	3	2	1	1	296.02	340.05
64	16	3	3	2	1	1	293.05	334.04
64	32	3	3	2	1	1	292.81	332.90
results (Winters *et al.* 1988)							291.52	330.76
32	16	3	3	3	1	1	261.81	315.40
64	16	3	3	3	1	1	256.40	305.02
128	16	3	3	3	1	1	255.07	302.50
results (Winters *et al.* 1988)							254.00	300.71
32	8	3	3	4	20	1	890.47	910.84
64	16	3	3	4	20	1	843.89	851.99
128	32	3	3	4	20	1	832.17	837.86
results (Van de Vooren & Dykstra 1989)							826	831

TABLE 1. Values of Ma_0 for the first two primary bifurcation points on different grids (n, m) for various values of Bi, ϵ and A. The quantities q_x and q_z are stretching parameters. If the value of a stretching parameter is 1, the grid is equidistant.

applying the boundary conditions which have to be satisfied by each member of the symmetry class at $x = \frac{1}{2}A$. Let $\vartheta = T - \bar{T}$, then these boundary conditions are:

$$\text{For } \psi \text{ even and } \vartheta \text{ odd}: \quad \psi_x = \omega_x = \vartheta = 0, \tag{9a}$$

$$\text{For } \psi \text{ odd and } \vartheta \text{ even}: \quad \psi = \omega = \vartheta_x = 0. \tag{9b}$$

The system of linear equations after Newton linearization of (8) was solved along the guidelines given by Werner & Spence (1980) through the decoupling of the linear systems. A starting point and starting tangent were found in the same way as was done in the limit point continuation.

5. Justification of numerical solutions

Values of Ma_0 at the first two primary bifurcation points (Ma_{01}, Ma_{02}) calculated with different (non-equidistant) grids were compared with existing analytic and other numerical results. In table 1, the results of these grid studies are shown in comparison with work in Winters *et al.* (1988) and Van de Vooren & Dijkstra (1988). It is observed that a $32^*A \times 16$ grid gives sufficient accuracy in the primary bifurcation points and these grids were used in most of the computations below. In addition, if $\epsilon = 0$ the choice $q_x = 1, q_z = 3$ is adequate whereas for $\epsilon = 1$ the choice $q_x = 3, q_z = 3$ gives better results.

In the nonlinear regime, solutions at a particular branch were compared with

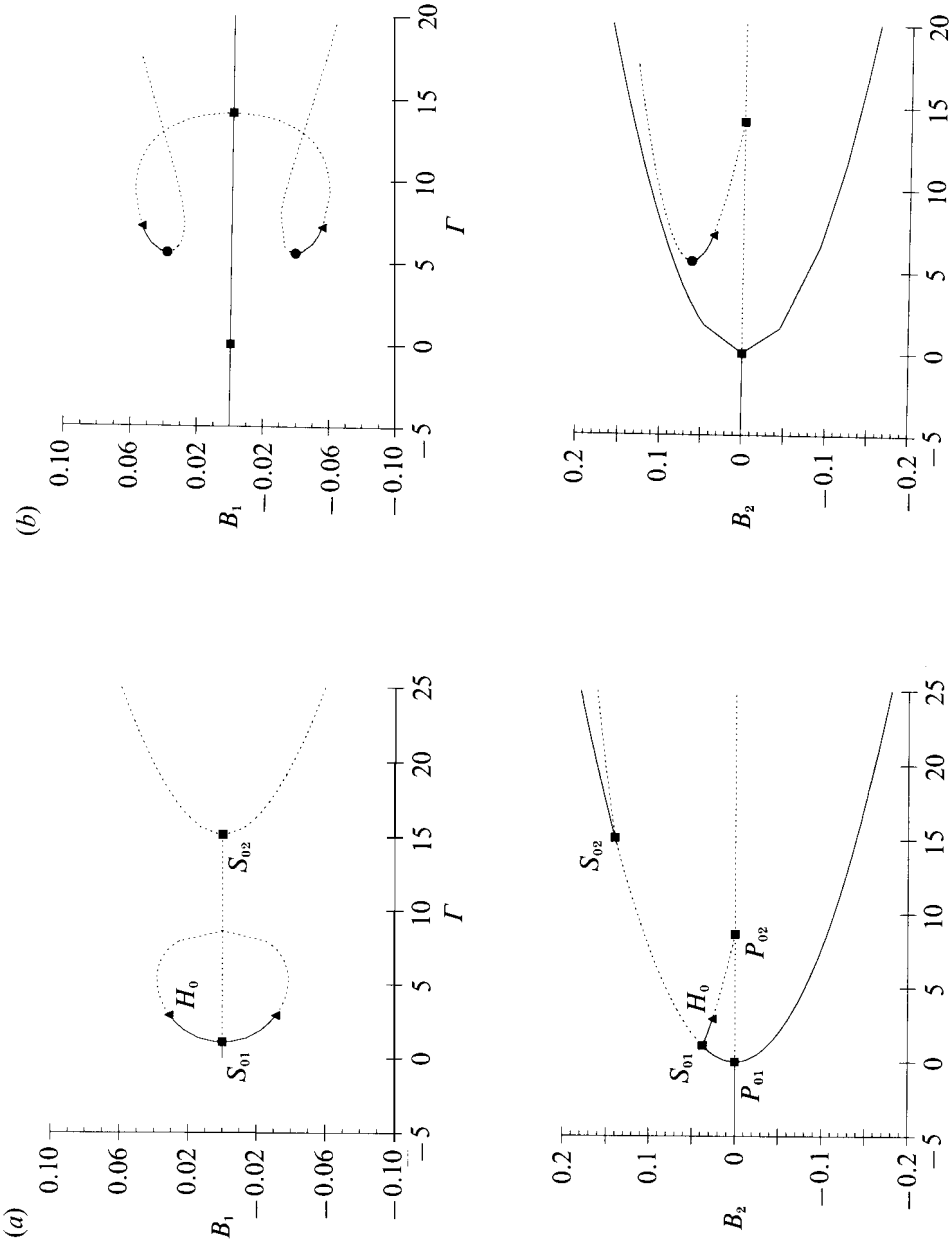

FIGURE 3. Bifurcation diagram for $\epsilon = 0$, $Bi = 0$, $Pr = 10$ and (*a*) $A = 2.4$ and (*b*) $A = 2.5$, calculated using the amplitude equations (10). ——, Stable branches; – – –, unstable branches.

Type of singularity/grid	32×16	64×16	Amplitude equations (10)
P_{01}	87.71	87.25	86.73
P_{02}	95.72	95.57	95.36
S_{01}	89.39	88.87	87.83
S_{02}	104.18	100.83	101.86
H_0	90.66	90.15	89.61

TABLE 2. Comparison of the values of Ma at singularities in the bifurcation pictures in figure 3(*a*) $A = 2.4$, $Bi = 0$, $Ra_0 = 0$, $\epsilon = 0$, $q_x = 1$, $q_z = 3$ and $Pr = 10$

solutions obtained from a transient code as reported in Dijkstra & Van de Vooren (1989). Unfortunately, we cannot compare our results directly with those in Winters *et al.* (1988), because the value of Pr used in these calculations is not reported.

The comparison of our numerical results and the results from local bifurcation analysis reported in Rosenblat *et al.* (1982) is presented in more detail for later reference. Focus is on the case $Bi = 0$, $Pr = 10$ and A near the double point at $A_0^0 = 2.25$. At this point the 1- and 2-cell patterns compete. A weakly nonlinear analysis provides the following amplitude equations (Rosenblat *et al.* 1982)

$$B_1' = c_1[\Gamma - (\theta+1)\Delta]B_1 + c_2 B_1 B_2 - c_3 B_1^3 - c_4 B_1 B_2^2, \tag{10a}$$

$$B_2' = d_1[\Gamma + (1-\theta)\Delta]B_2 - d_2 B_1^2 - d_3 B_1^2 B_2 - d_4 B_2^3, \tag{10b}$$

where the B_1 and B_2 represent the amplitude of the competing 1-cell and 2-cell patterns and the coefficients c_i, d_i are all positive. Furthermore, $\Delta = \frac{1}{2}(Ma_1 - Ma_2)$, i.e. half the difference of values of Ma at primary bifurcation points (at a chosen A), Γ measures the distance from onset and $\theta = \text{sign}\,(A - A_0^0)$. The numerical values of the c_i, d_i depend on Pr and are presented in table 3 of Rosenblat *et al.* (1982).

The bifurcation structure of (10) was determined numerically with standard ODE-bifurcation software. For $A = 2.4$ and $A = 2.5$ the amplitudes of the B_i are shown as a function of Γ in the figures 3(*a*) and 3(*b*), respectively. In these figures primary, secondary and Hopf bifurcations are indicated by the labels P, S and H, respectively. Figure 3(*a*) ($A = 2.4$) looks indeed like the sketch in figure 9 of Rosenblat *et al.* (1982). However, there is an additional bifurcation point (S_{02}) stabilizing the 2-cell pattern at larger Γ which was not shown in Rosenblat *et al.* (1982). S_{01} and S_{02} move towards each other with increasing A, coalesce and at $A = 2.5$ (figure 3*b*) the secondary branches no longer connect. This transition will be referred to below.

The values of Ma at the singularities for $A = 2.4$ calculated from (10) are compared in table 2 with those calculated using the numerical methods described in the previous section. The agreement is satisfactory and the amplitude equations have indeed a surprisingly large domain of validity. It seems that the local theory is valid up to $A = 2.4$ and up to $Ma = 100$. Furthermore, these figures also explain the apparent disagreement we previously reported in Dijkstra & Van de Vooren (1989); the amplitude equations had not been explored fully in Rosenblat *et al.* (1982).

6. Results

The results are presented in the form of bifurcation plots, with Ma_0 on the horizontal axis and a quantity W on the vertical axis. Here W is the value of the vertical velocity at the specific gridpoint $(\frac{1}{8}n, \frac{1}{2}m)$. Solid lines indicate stable branches,

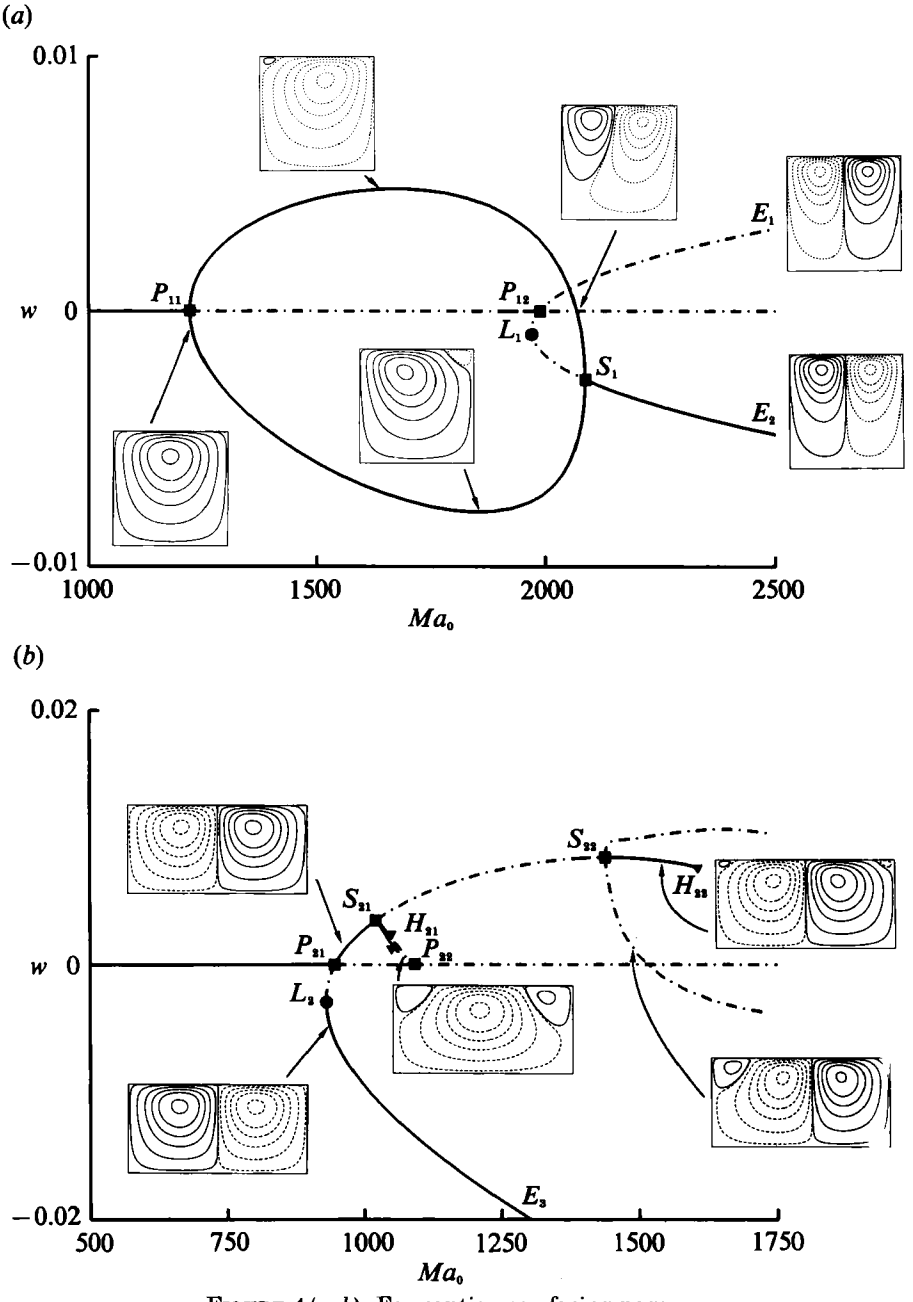

FIGURE 4(*a*, *b*). For caption see facing page.

while dash–dot lines indicate unstable branches. For all the singularities on the branches shown in each bifurcation picture those labelled with a P, S, L and H are primary bifurcation points, secondary bifurcation points, limit points (saddle node bifurcations) and Hopf bifurcation points, respectively. Sometimes E is used to denote a computational endpoint of a particular branch in the plot.

The patterns shown in the figures are contour plots of the streamfunction. If Ψ_m is the maximum of the streamfunction on the grid, then the solid contour lines are

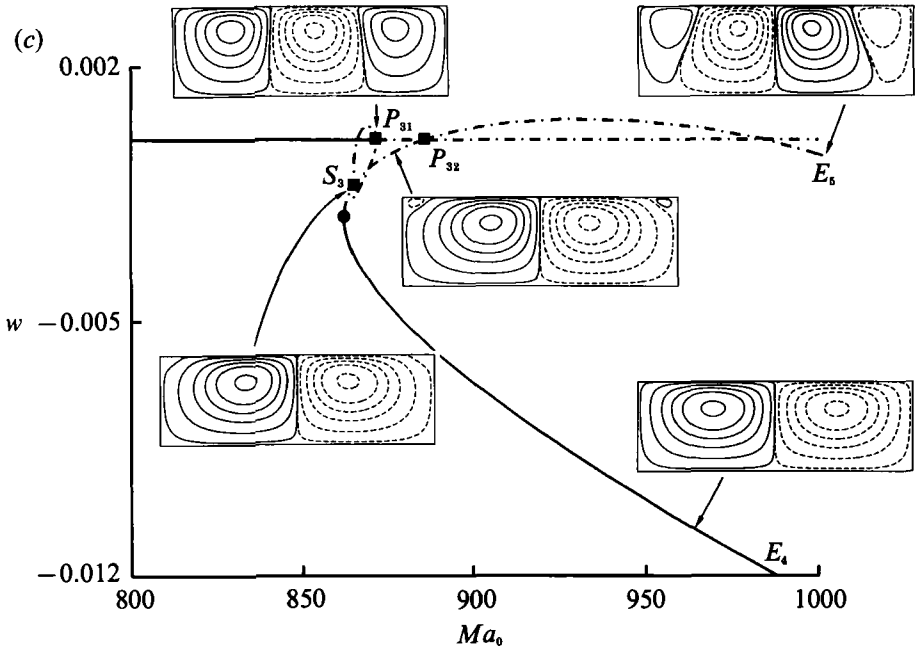

FIGURE 4. Bifurcation diagrams and flow patterns of steady solutions for $\epsilon = 1$, $Bi = 20$ and $Pr = 8$. (*a*) $A = 1$, (*b*) $A = 2$, (*c*) $A = 3$.

at levels 0.95, 0.7, 0.5, 0.3, 0.1, 0.001 of the value of Ψ_m. The dashed lines connect negative streamfunction values at the same levels as the solid lines.

6.1. *Bifurcation structure for rigid sidewalls; $Bi = 20$, $Ra_0 = 0$, $Pr = 8$*

The structure of steady solutions for a square container ($A = 1$) is shown in figure 4(*a*). At P_{11} there is a pitchfork bifurcation, two 1-cell patterns stabilize as the motionless solution gets unstable. On the upper branch $P_{11}-S_1$ the stable pattern near P_{11} consists of a clockwise rotating cell. With increasing Ma_0, a second cell develops in the upper left-hand corner and grows as S_1 is approached. At S_1 the pattern consists of two cells with centre upflow, which is, for further reference, indicated by the 2_u-cell pattern. The pattern change along the lower branch $P_{11}-S_1$ is just the image (under the reflection through $x = \frac{1}{2}A$) of that of the upper branch $P_{11}-S_1$; this gives again the 2_u-cell pattern at S_1. At P_{12}, a transcritical bifurcation point, two unstable 2-cell patterns branch off. Whereas the branch $P_{12}-E_1$ consisting of a 2-cell pattern with centre downflow (from now on the 2_d-cell pattern) remains unstable, the 2_u-cell pattern stabilizes at the secondary bifurcation point S_1. Considering realizable (i.e. linearly stable) flow patterns, there is a gradual transition from one of the 1-cell patterns to the 2_u-cell pattern (with increasing Ma_0).

Inspection of figure 2(*b*) shows that as the aspect ratio increases the primary bifurcation points P_{11} and P_{12} of figure 4(*a*) move towards each other and at $A_1^1 \approx 1.74$, they coalesce. Since the type of bifurcation is not changed as A crosses A_1^1, the primary bifurcation point P_{21} in the bifurcation structure for $A = 2$ (figure 4*b*) is a transcritical bifurcation point whereas P_{22} is a subcritical pitchfork. Along the branch $P_{21}-E_3$, the 2_u-cell pattern now stabilizes after L_2. Since the Ma_0 value of L_2 is smaller than that of P_{21}, there is stable steady convection below onset. Along the branch $P_{21}-S_{21}$, the 2_d-cell pattern is stable. After becoming unstable at S_{21}, it regains stability at S_{22} where two small cells appear in the upper corners. Finally, this

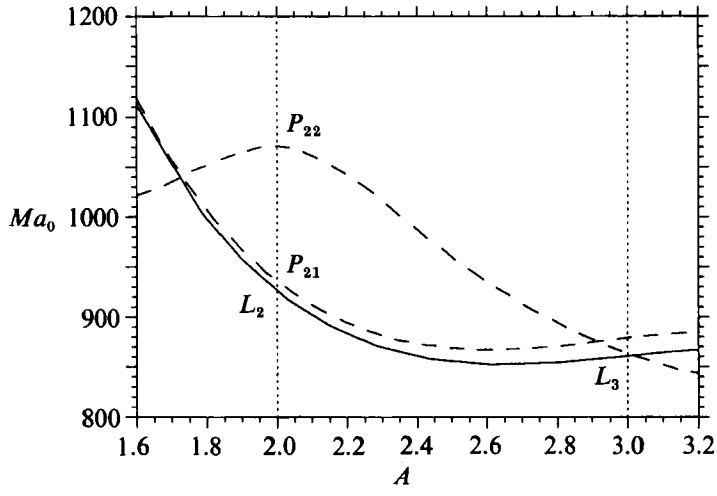

FIGURE 5. The paths of primary bifurcation points P_{21} and P_{22} and the limit point L_2 (see figure 4*b*) as a function of A for $Ra_0 = 0$, $Bi = 20$ and $Pr = 8$.

solution becomes unstable through a Hopf-bifurcation at H_{22}. At P_{22}, two $\mathbb{Z}_2$-related unstable 3-cell patterns branch off subcritically. Along each branch, a cell in the upper corner decays, whereas the one in the other corner grows. These solutions stabilize through a Hopf-bifurcation at H_{21}, and are connected at S_{21} to the 2_d-cell pattern. Additional branches appear at the third primary bifurcation point at $Ma_0 = 1401.6$, but remain unstable (up to $Ma_0 = 1700$) and are not shown.

The primary bifurcation points interchange again at $A_2^1 \approx 2.94$. In the bifurcation picture of $A = 3$ (figure 4*c*) the first primary bifurcation point P_{31} is a pitchfork and P_{32} is transcritical. There is still stable convection below onset, because the Ma_0 value at L_3 is smaller than that of P_{31}. The pattern change along the unstable branch $P_{31}-S_3$ is basically the same as along the branch $P_{22}-S_{21}$ in figure 4(*b*) except that the two corner cells are relatively larger. Along the branch $P_{32}-S_3-L_3-E_4$ the two corner cells, present near P_{32}, disappear as the solution stabilizes. Along the branch $P_{32}-E_5$ the corner cells grow to a 4-cell pattern, which remains unstable up to $Ma_0 = 1000$.

6.2. *Hysteresis*

Stable convection below onset, which gives rise to hysteresis effects, occurred at $A = 2$ (figure 4*b*) and $A = 3$ (figure 4*c*). The complete range of aspect ratio where hysteresis occurs is shown in figure 5. The path of the limit point L_2 (in figure 4*b*) was continued on a 128×16 grid and the values of the points P were taken from Van de Vooren & Dijkstra (1989) (these are extrapolated values). Hysteresis becomes approximately non-zero at the first double point A_1^1, increases with A until the next double point A_2^1 and vanishes slightly above $A = 3.0$. It is known (Davis 1987) that for a layer of infinite horizontal extent ($A \to \infty$), a region of subcritical instabilities is possible for pure Marangoni convection, because the energy stability limit is smaller than the linear stability limit. Here, this region is restricted to a particular range in aspect ratio. Note that the neutral curve structure is very important in this respect. The limit point follows the path of the primary bifurcation point P_{21} and therefore the region in aspect ratio where hysteresis occurs is well approximated by the region between the double points ($A_2^1-A_1^1$).

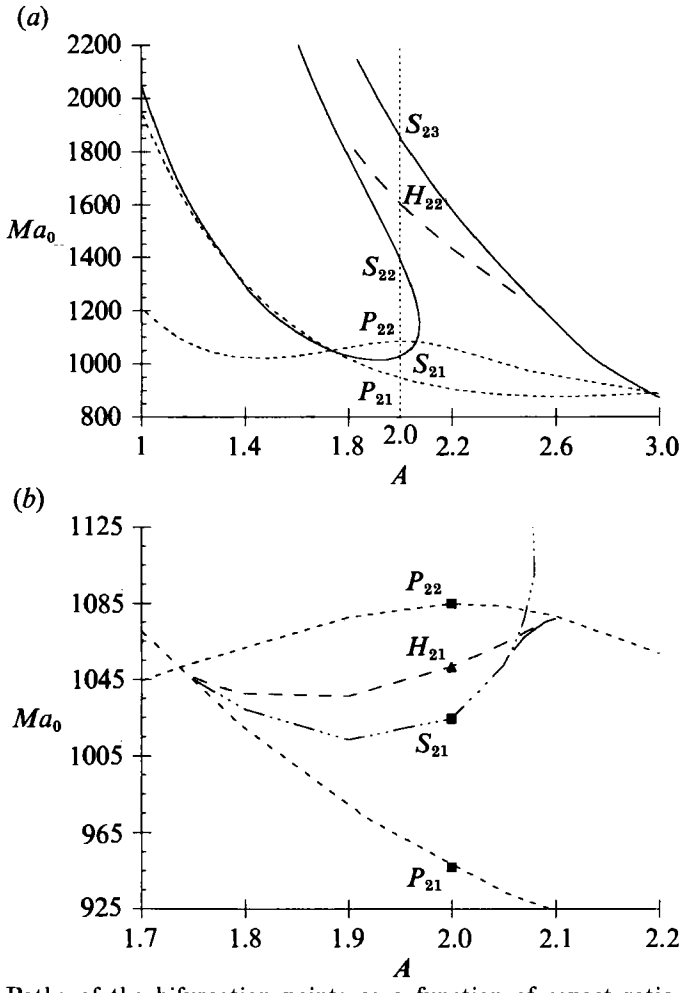

FIGURE 6. Paths of the bifurcation points as a function of aspect ratio A. For clearness, the intersection of the vertical line with the curves are bifurcation points in figure 4(*b*). (*b*) Closeup of (*a*) near $A = 2.0$. The (short) solid curve in (*b*) is a branch of limit points.

6.3. *Modal exchange*

How do the pictures of figures 4(*a*), 4(*b*) and 4(*c*) transform into each other as the aspect ratio is varied? In particular, how do the positions of the bifurcation points change with A? To answer these questions the paths of primary bifurcation points P and secondary bifurcation points S were calculated as a function of aspect ratio. The change of the Hopf bifurcation points H with A was calculated as follows. First a regular point nearby H was continued in A up to a prescribed value of A. Thereafter the point H at this new value of A was detected in the usual way. Results are shown in figure 6 for a 64×16 grid. Figure 6(*b*) is a close up of a part of figure 6(*a*).

From $A = 1$ up to $A_1^1 = 1.74$, the qualitative bifurcation picture is the same as figure 4(*a*). At $A = A_1^1$, the two primary bifurcation points P_{11} and P_{12} and the secondary bifurcation point S_1 of figure 4(*a*) intersect. The unfolding of this singularity (cf. Guckenheimer & Holmes 1983, pp. 364–376) for $A - A_1^1 > 0$ gives a secondary bifurcation point and a Hopf bifurcation point which move (figure 6*b*) with increasing A to the points S_{21} and H_{21} at $A = 2$.

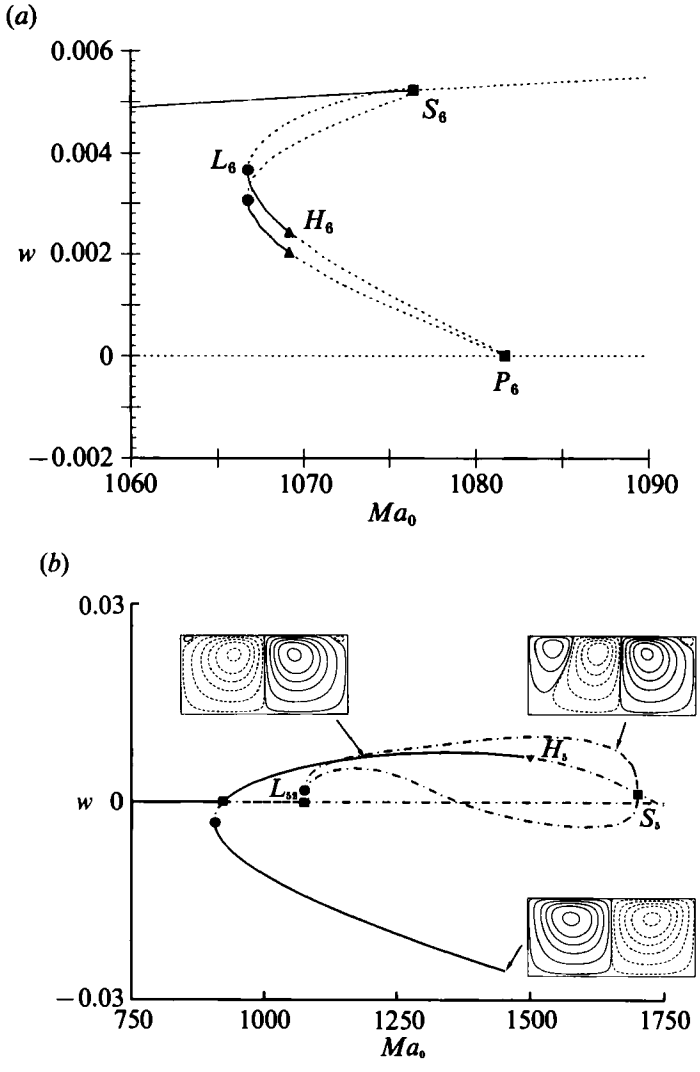

FIGURE 7. Bifurcation pictures for $\epsilon = 1$, $Ra_0 = 0$, $Bi = 20$, $Pr = 8$. (*a*) $A = 2.07$, (*b*) $A = 2.1$. Again solid curves indicate stable branches.

In figure 4(*b*), new singularities have appeared within the computational range, i.e. the secondary bifurcation point S_{22} and the Hopf bifurcation point H_{22}. Figure 6(*a*) shows that S_{21} and S_{22} move towards each other with increasing A and finally coalesce at $A_3^1 \approx 2.085$. The detailed picture of the transition near this point is shown in figure 6(*b*). The continuation of the branch $P_{22}-H_{21}-S_{21}$ (figure 4*b*) to $A = 2.07$ is shown in figure 7(*a*). Two additional limit points (L_6) are observed, whereas P_{21}, H_{21} and S_{21} have moved to P_6, H_6 and S_6, respectively. These limit points appear near $A = 2.06$ (figure 6*b*). The intersection of the paths of S_{21} and S_{22} (at A_3^1) is (numerically) close to the intersection point of the paths of L_6 and H_6. Near A_3^1, the Hopf bifurcations disappear.

The new qualitative behaviour is seen in figure 7(*b*), where the bifurcation picture for $A = 2.1$ is plotted. The limit points L_6 in figure 7(*a*) have moved to the points L_{52} in figure 7(*b*). The Hopf bifurcation point H_{22} in figure 4(*b*) has moved to H_5. The

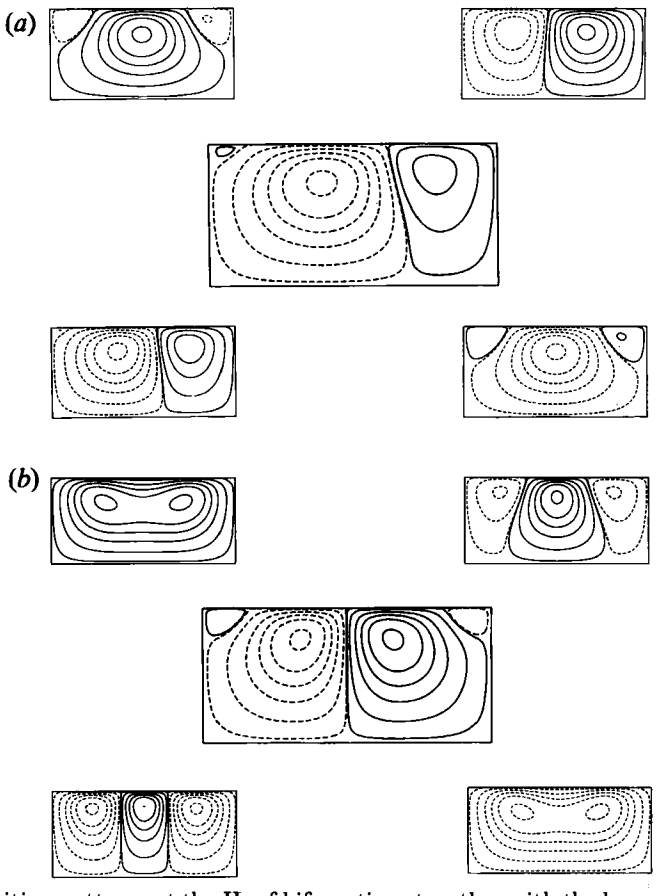

FIGURE 8. Transition patterns at the Hopf bifurcations together with the base state (larger picture in the middle). The time is in units π/ω_0 and $t = 0$ in the figure top left-hand side, $t = 0.25$ in the figure top right-hand side, $t = 0.75$ in the figure bottom left-hand side and $t = 1$ in the figure bottom right-hand side. (*a*) $A = 2.0$, $Ma_0 = 1051.5$, $\omega_0 = 5.92 \times 10^{-3}$ at H_{21} (in figure 4*b*). (*b*) $A = 2.1$, $Ma_0 = 1513.9$, $\omega_0 = 2.70 \times 10^{-2}$ at H_5 (in figure 7*b*).

branches through L_{52} now connect to the secondary bifurcation point S_5 (figure 7*b*) which now appears within the computational range.

The path of the points S_5 and H_{22} are also shown in figure 6(*a*). At $A_4^1 \approx 2.5$, these paths coalesce and the Hopf bifurcation points thereby disappear. The Hopf bifurcation points disappear in the same way at $A_5^1 \approx 1.8$ where the paths of H_{22} and the secondary bifurcation point S_{22} (figure 4*b*) coalesce. At the double point $A_2^1 = 2.94$, S_5 crosses the primary branch to give the picture in figure 4(*c*).

In summary, in figure 6 there are several higher codimension ($\geqslant 2$) bifurcations. At A_1^1 and A_2^1 there is a steady state/steady mode interaction (or a double zero eigenvalue). At A_4^1 and A_5^1 there is a Hopf/steady state mode interaction (or a pure imaginary pair and a zero eigenvalue). The results indicate that at A_3^1 a global bifurcation occurs.

6.4. *Transition to time-dependent flow near aspect ratio* 2

Time-periodic convection patterns branch off near the detected Hopf bifurcation points. The spatial structure of these periodic solutions close to onset can be determined by investigation of the eigenvectors (w_1, w_2) corresponding to the pair of

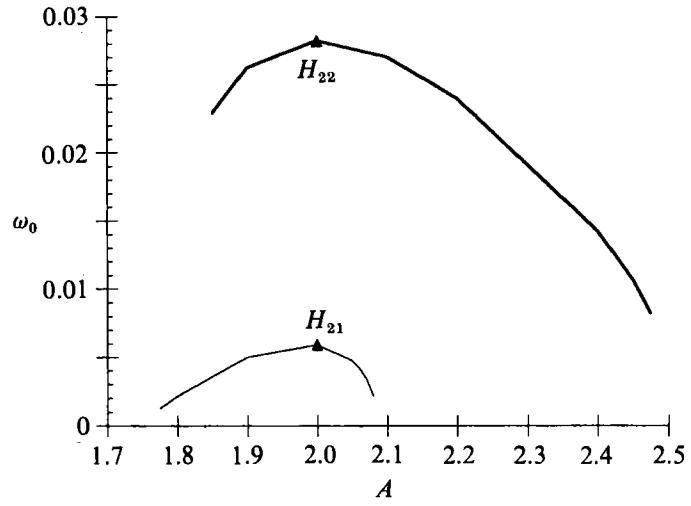

FIGURE 9. Frequency ω_0 along the paths of the Hopf-bifurcations H_{21} and H_{22} in figure 6.

eigenvalues ($\pm i\omega_0$) which cross the imaginary axis. This time periodic structure is referred to as the transition state and given by

$$\phi(t) = \sin(\omega_0 t)\, w_1 + \cos(\omega_0 t)\, w_2, t \in [0,\ 2\pi/\omega_0]. \tag{11}$$

In figure 8(a), contours of the streamfunction are plotted for several times t (in units π/ω_0) for the transition state at the point H_{21} (figure 4b) at $Ma_0 = 1051.5$; the steady base state is also shown (the bigger picture). In figure 8(b), the transition structure is plotted for the point H_5 (figure 7b) at $Ma_0 = 1513.9$. The transition structure at H_{22} (figure 4b) at $Ma_0 = 1609.9$ is very similar to that in figure 8(b). Values of the angular frequencies ω_0 are presented in the captions.

The periodic disturbance in figure 8(a) is seen to be composed of an interaction of two patterns, the pattern shown for $t = 0$ and the 2-cell centre downflow pattern. In figure 8(b) this competition is also apparent and one pattern consists of 1 cell, the other of 3 cells.

To find a periodic solution of the full nonlinear equations near the point H_{21}, trajectories were computed using the second-order Crank–Nicolson scheme used in Dijkstra (1988). (It turns out that a timestep of $\frac{1}{20}$ of the period ($2\pi/\omega_0$) is sufficient to obtain accurate solutions.) The initial conditions consist of a superposition of the base state at H_{21} and the transition structure multiplied by some small amplitude. A stable periodic solution is found near $Ma_0 = 1051.5$. This flow consists of a small oscillation of the cells in the container, where the right-hand cell (figure 8(a), steady state) becomes slightly larger and the left-hand small cell slightly smaller over half a period. The maximum velocity of the base state is about $10^{-2}\,\kappa/\mathrm{H}$ (m s^{-1}), whereas the mean velocity q_m along the (big) middle cell is about $5.0 \times 10^{-3}\,\kappa/\mathrm{H}$ (m s^{-1}). A typical circulation time along this big cell is therefore $\pi H/q_m \approx 2\pi\ 10^2\ \mathrm{H}^2/\kappa$ (s). The period of the oscillatory solution is $2\pi/\omega_0\ \mathrm{H}^2/\kappa$ (s) near the onset of periodic flow. With $\omega_0 = 5.92 \times 10^{-3}$, this period has the same order of magnitude as a typical circulation time.

The dependence of the angular frequency on Ma_0 along the paths of Hopf bifurcation points in figure 6(a) and figure 6(b), respectively is shown in figure 9. Initially this frequency increases with A and reaches a maximum near $A = 2$, thereafter it decreases with A until the branch ends. The angular frequency $\omega_0 \to 0$ as $A \downarrow A_1^1$. Hence the Hopf bifurcation arises from the unfolding of the double point

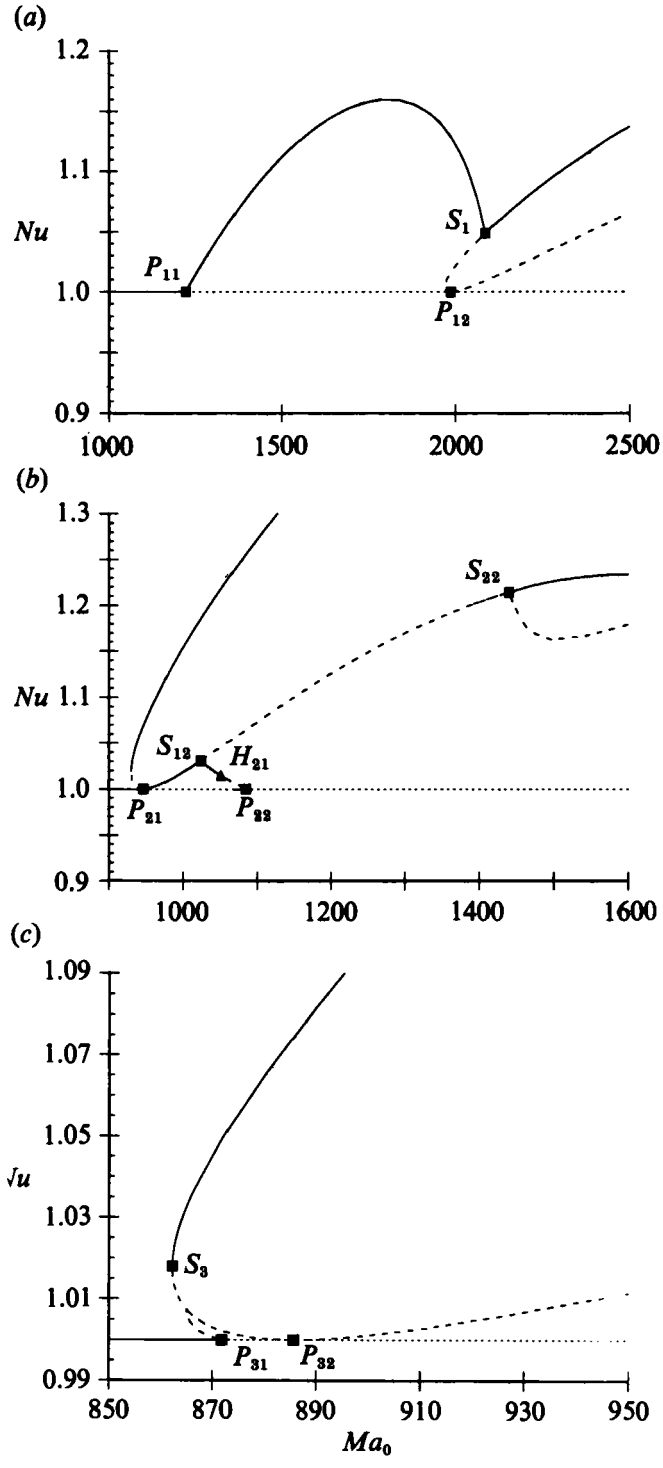

FIGURE 10. Nusselt number Nu as a function of Ma_0 for the steady solutions along the branches of figure 4. (*a*) $A = 1$, (*b*) $A = 2$, (*c*) $A = 3$.

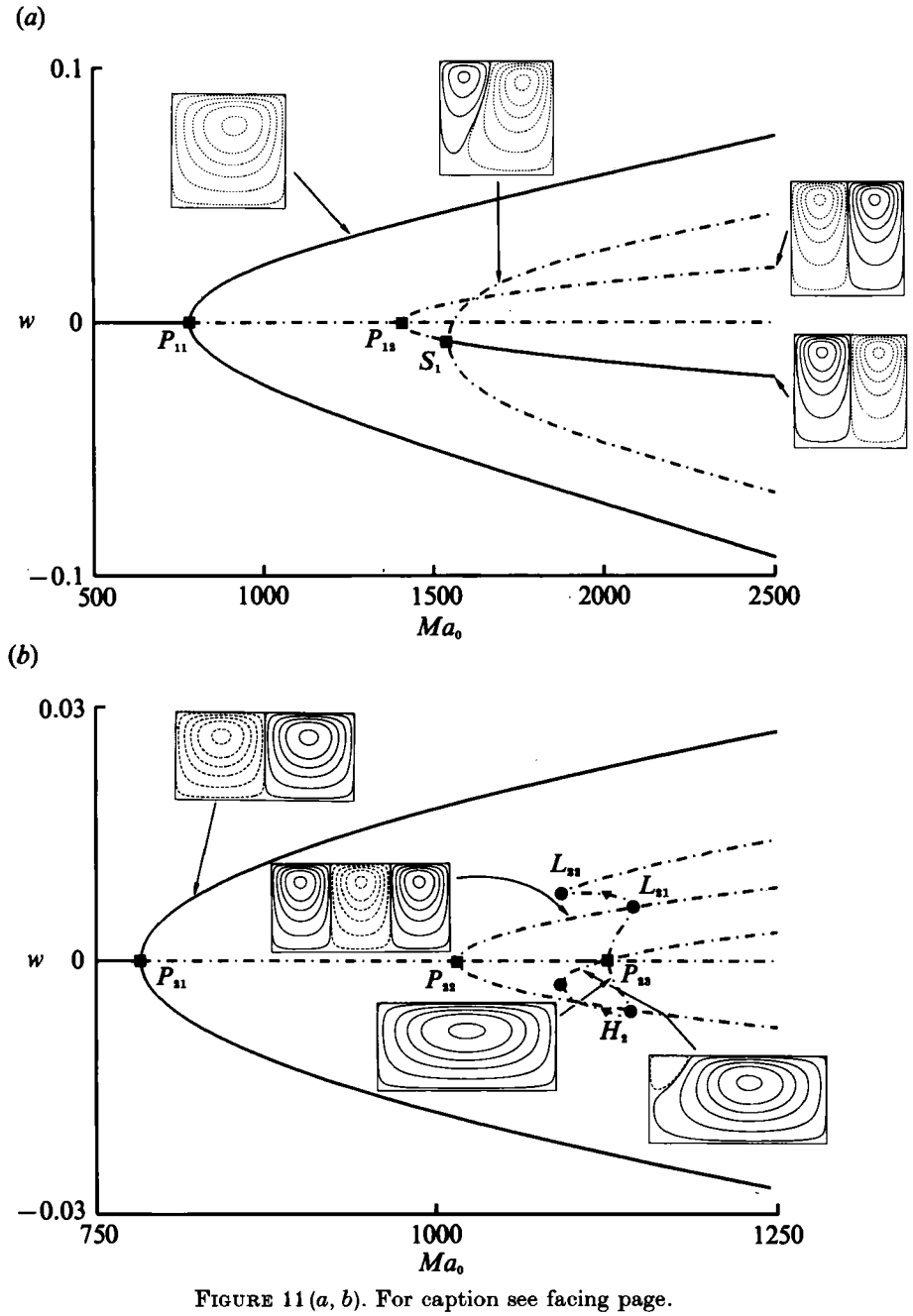

FIGURE 11 (*a*, *b*). For caption see facing page.

singularity and is not already present at the primary branch (i.e. the principle of exchange of stabilities is valid).

6.5. *Heat transport*

The Nusselt number Nu along the branches of figure 4 are presented in figure 10. It is defined as

$$Nu = \frac{Bi+1}{ABi}\int_0^A \left(wT - \frac{\partial T}{\partial z}\right)\mathrm{d}x. \tag{12}$$

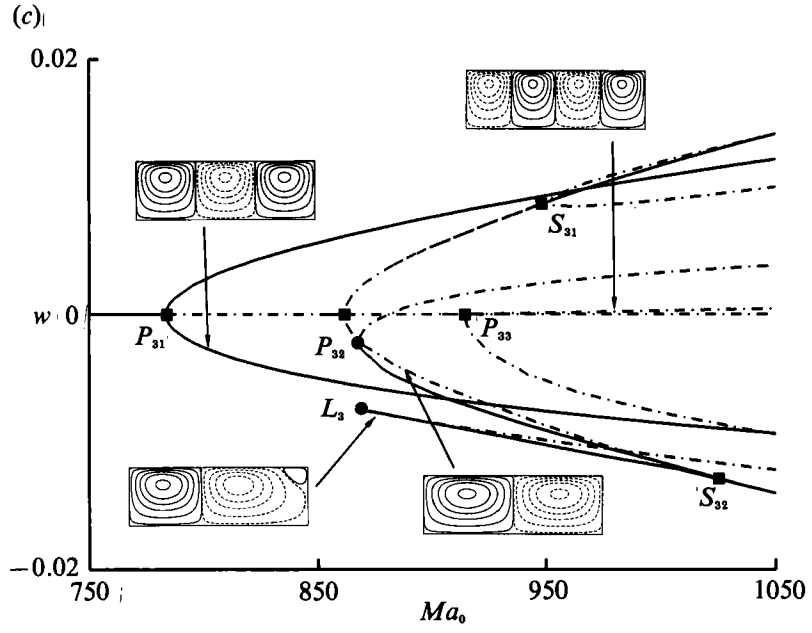

FIGURE 11. Bifurcation diagrams and flow patterns of steady solutions for 'slippery' sidewalls ($\epsilon = 0$), $Bi = 20$ and $Pr = 8$. (*a*) $A = 1$, (*b*) $A = 2$, (*c*) $A = 3$.

As is well known, the Nusselt number is a measure of the increase in heat flux due to convection. In our calculations, the difference in Nu between the top free surface and the bottom wall for a particular steady state is smaller than 1%; $\mathbb{Z}_2$-related patterns have the same value of Nu.

In most cases, the stable solutions have larger values of Nu than unstable ones. In addition, the 2_u-cell pattern has the largest value of Nu in figures 10(*b*) and 10(*c*). There is a slight decrease in heat transport in figure 10(*a*), accompanying the continuous transition from the 1-cell patterns to the 2_u-cell pattern. This indicates that the occurrence of the corner cells decreases the heat transport.

7. The influence of the type of lateral walls and secondary parameters

7.1. *'Slippery' sidewalls*

The multiplicity of stable and unstable patterns for a container having 'slippery' sidewalls is considered next. For standard values of the parameters ($Ra_0 = 0$, $Bi = 20$, $Pr = 8$) the bifurcation pictures for aspect ratio 1, 2 and 3 are presented in the figures 11(*a*)–11(*c*), respectively.

Comparing the results for 'no-slip' sidewalls (figures 2*b* and 4) with those for 'slippery' sidewalls (figures 2*a* and 11), the following is observed:

(i) The critical Marangoni numbers at onset are larger for 'no-slip' sidewalls and therefore the 'no-slip' condition stabilizes the conduction solution (3).

(ii) Transcritical primary bifurcation points occur in the 'no-slip' case when an even number of cells branches off. This is due to the trivial action of the $\mathbb{Z}_2$-symmetry at these points. All bifurcation points are of pitchfork type for 'slippery' sidewalls because of the additional translational symmetry which is broken. Hence, subcritical convection is absent for 'slippery' sidewalls.

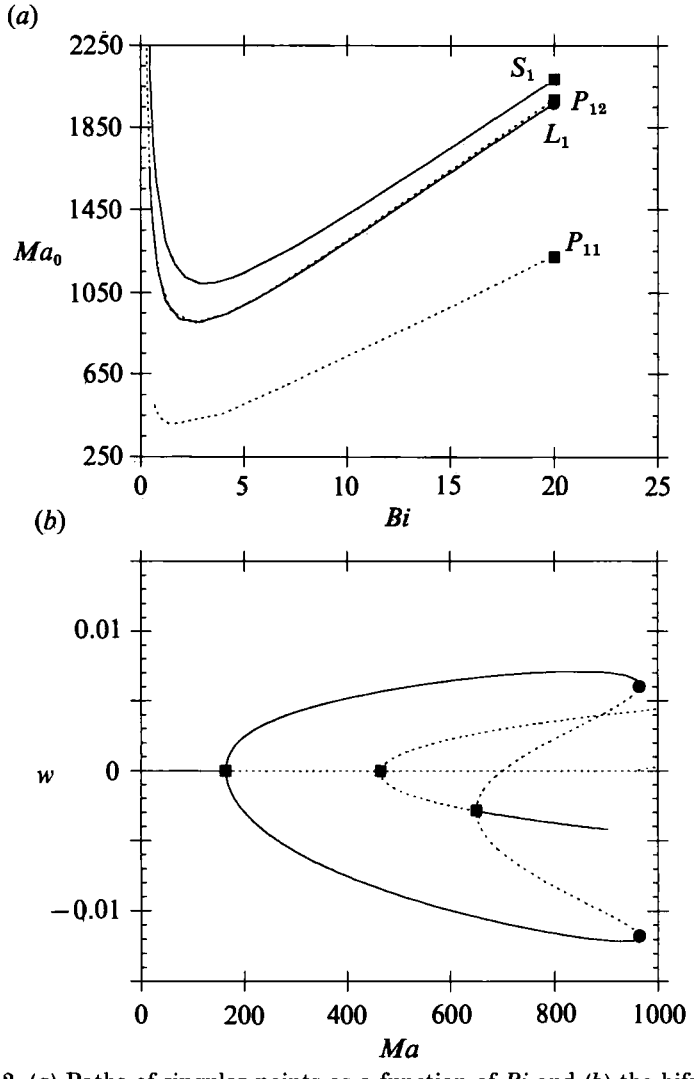

FIGURE 12. (a) Paths of singular points as a function of Bi and (b) the bifurcation picture for $Bi = 0$ for $A = 1$, $Pr = 8$ and $Ra_0 = 0$.

(iii) The double points at onset, where two modes compete, occur at larger aspect ratio in the 'no-slip' case.

(iv) Double points, where both solutions have the same $\mathbb{Z}_2$-symmetry (e.g. a 1-cell and 3-cell pattern) disappear in the 'no-slip' case.

(v) The multiplicity of stable patterns is smaller in the 'no-slip' case. This is due to the occurrence of additional limit points and closed branches.

The change of bifurcation pictures with aspect ratio (in figure 11) can be understood with reference to the results in Rosenblat *et al.* (1982) and figure 3 of this paper. We discuss only the modal exchange at the first double point at $A_1^0 = 1.56$. From $A = 1$ up to A_1^0, S_1 (in figure 11*a*) moves towards the primary branch, crossing this branch exactly at the double point. For A slightly less than A_1^0, the bifurcation picture is qualitatively the same as figure 8 in Rosenblat *et al.* (1982). Slightly above A_1^0, the bifurcation picture is qualitatively the same as figure 3(*a*) above. At larger

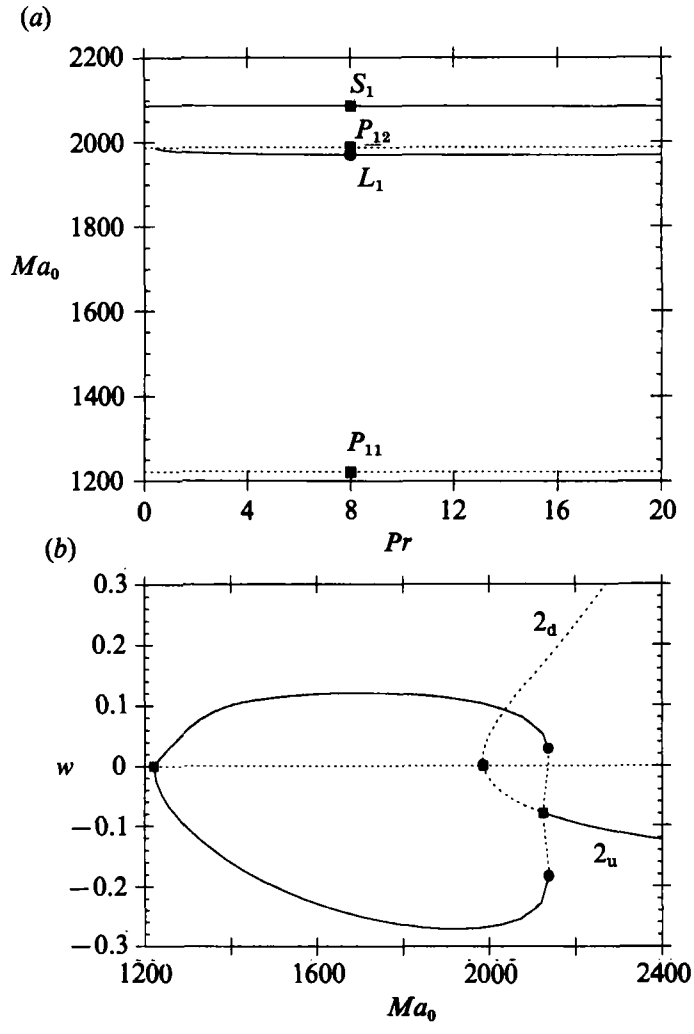

FIGURE 13. (*a*) Paths of singular points as a function of Pr for $A = 1$, $Bi = 20$ and $Ra_0 = 0$ and (*b*) the bifurcation picture for $Pr = 0.1$.

values of A, the two secondary bifurcation points (S_{01} and S_{02}, figure 3*a*) coalesce and the secondary branches disconnect as shown in figure 3(*b*). At this point there are two stable branches, consisting of 2-cell patterns (both centre upflow and centre downflow) as shown in figure 11(*b*). The structure of solutions becomes more complicated at $A = 3$ (figure 11*c*). Two $\mathbb{Z}_2$ related 3-cell patterns are stable over the computational range. Both (centre upflow and centre downflow) 2-cell solutions stabilize at the secondary bifurcation points S_{31} and S_{32}. From these points, two other stable mixed mode solutions appear which become unstable at the limit point L_3.

7.2. *Secondary parameters (rigid sidewalls)*

For a square container ($A = 1$) with 'no-slip' sidewalls, the paths of limit points and secondary bifurcation points are shown as a function of Bi in figure 12(*a*). The qualitative structure remains the same for each value of Bi. The distance between the paths of the points L_1 and P_{12} decreases with decreasing Bi and hence for small Bi

hysteresis is small. If one calculates the actual picture at $Bi = 0$, where W is shown now as a function of Ma (figure 12b), extra limit points are present. A small value of Bi causes the 1- and 2_u-cell patterns to be stable simultaneously. At large Bi this multiplicity of stable patterns disappears (cf. figure 4a).

Also for a square container, the paths of the relevant singularities are shown as a function of Pr in figure 13(a). Relatively little changes over the range 0.5–50, so the bifurcation structure remains qualitatively the same. At small Pr, the path of L_1 and that of P_{12} intersect. The bifurcation picture at $Pr = 0.1$ is shown in figure 13(b) and it indeed turns out that the limit point is now on the 2_d-cell branch. Furthermore, there is now also a slight range in Ma_0 where both the 2_u-cell and 1-cell patterns are stable. Hence both small Pr and small Bi promote multiple stable states to occur in a square container.

8. Discussion

By using techniques of numerical bifurcation theory the multiplicity and stability of cellular Marangoni flows was determined for small-aspect-ratio containers with two types of sidewalls. Within the computational domain considered, it is found that, for both type of sidewalls, multiple stable steady states do exist in certain regions of parameter space. For standard values of the secondary parameters ($Ra_0 = 0$, $Bi = 20$, $Pr = 8$) a composite figure showing the types of stable convection is given for 'no-slip' and 'slippery' sidewalls in figures 14(a) and 14(b), respectively. In both figures, open circles at the endpoints indicate the end of the computational domain whereas closed circles indicate singularities (transitions in stability). Clearly the 'no-slip' condition at the sidewalls causes the 2_u-cell pattern to be preferred over a large area in parameter space. This 'selection' process is complicated because of its origin in secondary effects, in particular the occurrence of limit points. It is also absent for 'slippery' sidewalls, where, at each integer value of the aspect ratio, several patterns are stable simultaneously.

Some physical insight into the occurrence of extra limit points for 'no-slip' sidewalls is obtained as follows. Using a simple two-dimensional model of buoyancy-driven convection, Drazin (1975) explained the difference between the onset eigenfunctions for $\epsilon = 0$ and $\epsilon = 1$. Whereas the x-dependence of the vertical velocity eigenfunctions are simple cosines for $\epsilon = 0$, those for $\epsilon = 1$ are a sum of 2 sinusoidal functions and a hyperbolic function. This hyperbolic function is exponentially small between the walls but accounts for the no-slip at the wall and hence introduces a 'boundary layer' (which might not be thin) along the walls. Consider now figure 4(a) ($\epsilon = 1, A = 1$). Along the upper branch $P_{11}-S_1$, the amplitude of the clockwise rotating 1-cell pattern increases. For this flow, the fluid elements are accelerated along the interface from left to right and therefore (at finite amplitude) the vertical velocity near $x = A$ is larger than near $x = 0$. This asymmetry increases with Ma_0, which can also be observed through the movement of the cell centre towards the right-hand wall. At some value of Ma_0, the horizontal gradient in vertical velocity will be influenced by the above mentioned 'boundary layer' and the downward movement along the right-hand wall is damped, thereby reducing the upward velocity near the left wall. The left-hand upper corner becomes relatively cool with respect to a point at the interface slightly to the right, which causes a flow to this corner and a small cell develops. In the same way, a small cell develops in the upper right-hand corner for the anti-clockwise rotating 1-cell flow along the lower branch $P_{11}-S_1$. Once these small cells are formed, either the pattern becomes unstable to the

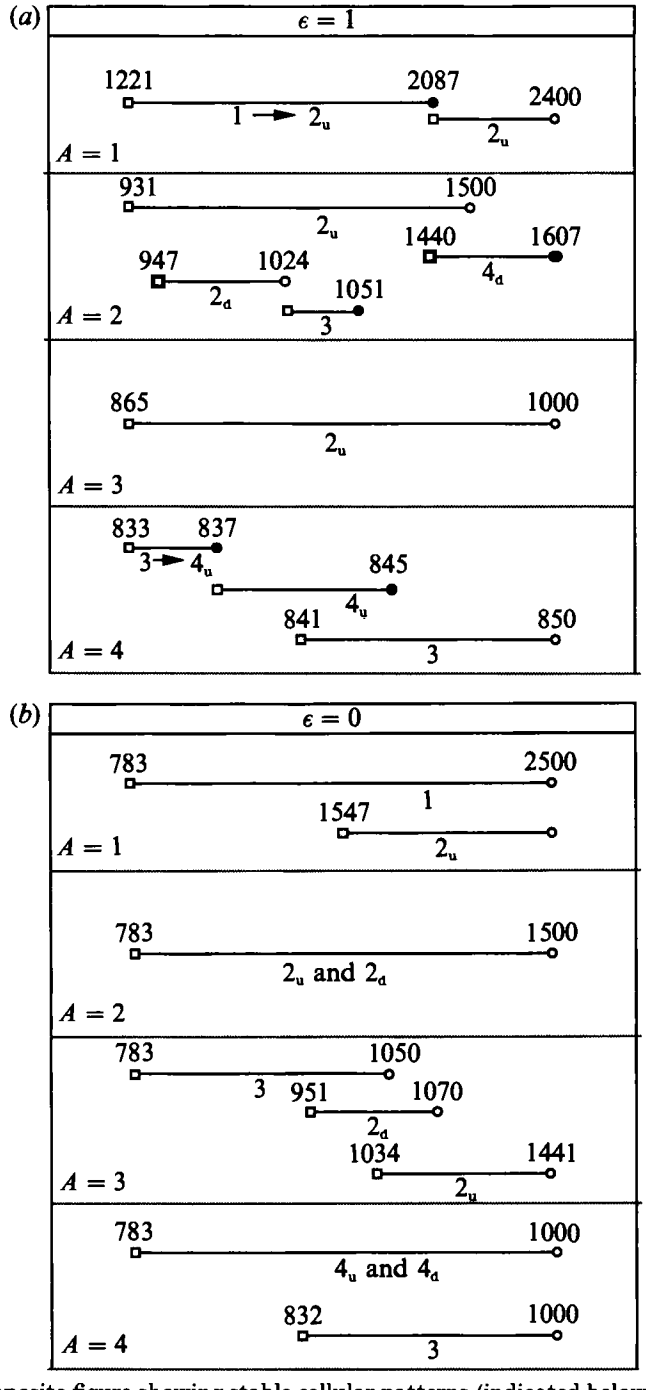

FIGURE 14. Composite figure showing stable cellular patterns (indicated below the lines) for integer aspect ratios both for (*a*) 'no-slip' and (*b*) 'slippery' sidewalls. Open circles indicate computational endpoints, whereas closed circles indicate a transition in stability.

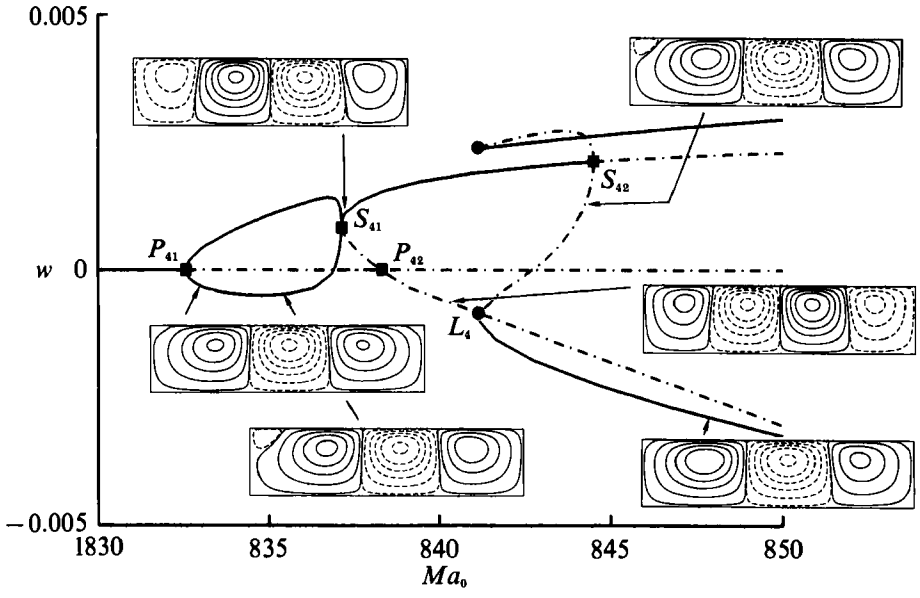

FIGURE 15. Bifurcation picture for 'no-slip' ($\epsilon = 1$) sidewalls and $Ra_0 = 0$, $Pr = 8$, $Bi = 20$ and $A = 4$.

2_u-cell pattern (which occurs for small Bi in figure 12b) or the small cell grows and the pattern remains stable (at large Bi). Hence, finally both $\mathbb{Z}_2$-related 1-cell patterns end up in the same secondary bifurcation point with a 2_u-cell pattern. Note that the small cells do not appear for $\epsilon = 0$, because the vertical velocity is non-zero at the sidewalls.

Similar reasoning explains the transition from the 3-cell pattern to the 4-cell pattern with centre upflow at $A = 4$ along the branch $P_{41}-S_{41}$ shown in figure 15. Another interesting point from this figure is that the 4-cell pattern becomes unstable at S_{42} whereas two $\mathbb{Z}_2$-related 3-cell patterns are stabilized at L_4. The wavelength of the preferred pattern thereby *increases* with increasing Ma_0.

It was demonstrated that transitions to time-dependent convection are possible close to onset (the path of H_{21} in figure 6b). The periodic solutions have their origin in steady state/steady state interactions. The period of oscillation has the same order of magnitude as a typical circulation time of the nearly steady state. Hopf bifurcation points also originate from Hopf/steady state interactions (the path of H_{22} in figure 6a).

To answer the question whether the bifurcation structure changes qualitatively if buoyancy is added, bifurcation structures for $Ma_0 = 0$ and $Bi = 1$ were calculated. The main reason to choose this value of Bi instead of $Bi = 20$ was that for the latter value the second primary bifurcation point occurs at large Ra_0 decreasing the numerical accuracy. In figure 16(a), the bifurcation picture (64×16 grid) is shown for $A = 2$. This picture just looks like figure 4(a), except that the second primary bifurcation point is a pitchfork instead of a transcritical bifurcation. It can be proved by local analysis that this is only true if $Ma_0 = 0$ and the pitchfork is therefore parameter induced (cf. Golubitsky & Schaeffer 1984, p. 324 ff). It turns out that the self-adjointness of the linear operator at $Ma_0 = 0$ is central in the proof. The absence of transcritical bifurcations implies that hysteresis is also absent. This is consistent with the infinite-layer results, where the energy stability limits and linear stability

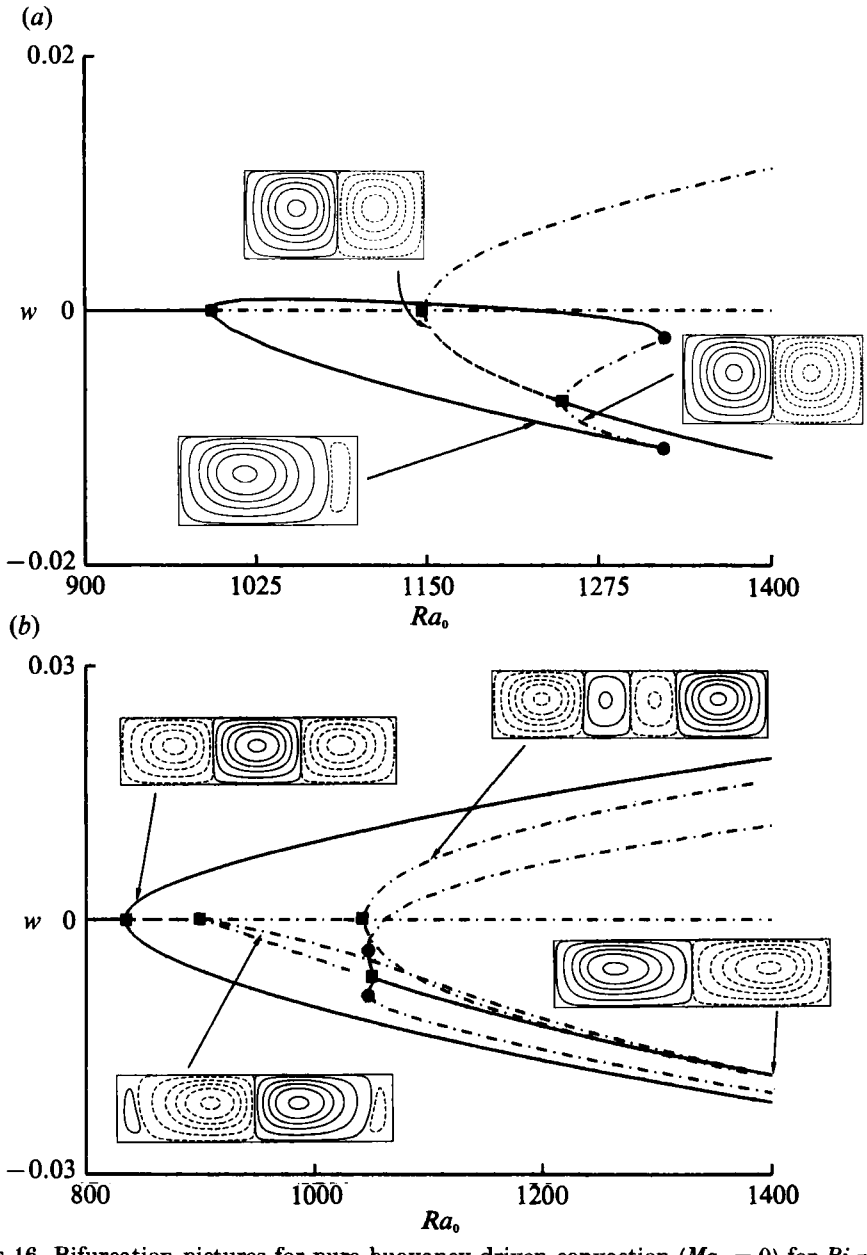

FIGURE 16. Bifurcation pictures for pure buoyancy driven convection ($Ma_0 = 0$) for $Bi = 1$ and $Pr = 8$. (*a*) $A = 2$, $\epsilon = 1$, (*b*) $A = 4$.

limits for buoyancy-driven convection are equal. Note that in the Rayleigh–Bénard case in a closed container with the same boundary conditions for velocity and temperature on the horizontal boundaries (as considered e.g. in Metzener 1986) all primary bifurcations are of pitchfork type because of the $\mathbb{Z}_2 \times \mathbb{Z}_2$ symmetry of the problem.

For $Bi = 1$, the first double point occurs at $A = 2.18$. For $A = 2.2$, the bifurcation structure is qualitatively the same as that in figure 3(*a*) (the Hopf bifurcation occurring at $Ra_0 = 2060$) and for $A = 2.25$ qualitatively the same as figure 3(*b*).

Hence the transition along the first double point is qualitatively the same as found for Marangoni convection. The bifurcation picture for $A = 4$ (128×16 grid) is shown in figure 16(*b*). Here both 3-cell patterns and the 2_u-cell pattern are stable far above onset. This picture looks more like one of the bifurcation pictures of figure 11 ($\epsilon = 0$) than of figure 4 ($\epsilon = 1$). This suggests that for this Bi and A the influence of the 'no-slip' sidewalls is less for pure buoyancy-driven than for pure surface-tension-driven convection.

What can we learn from these results with respect to experiments? Unfortunately, there are several factors which make a comparison with experimental work difficult. The geometry is different (cylindrical containers), the experimental aspect-ratio range is too large ($A \geqslant 5$), there is a rigid top wall (pure Rayleigh–Bénard convection) or three-dimensional effects are important (width of the container is not small). However, some features found in the calculations have also been observed in experiments.

The experimentally obtained critical temperature gradient for convection onset is always larger than that predicted by linear theory of the infinite layer and clearly due to the presence of sidewalls (Stork & Müller 1972; Koschmieder & Prahl 1990). Just above onset, there is in most cases a small region in parameter space where there is only one (or two $\mathbb{Z}_2$-related) stable pattern. Far above onset, multiple steady states are often observed and the change from one cell pattern to the other is often accompanied by hysteresis (Bergé 1975). The often observed (see e.g. Gollub & Benson 1980) increase in wavelength with increasing stability parameter might be due to secondary effects as in figure 15. Stable patterns with corner cells like those we found in figure 4(*b*) are reported by Gollub & Benson (1980). Bensimon (1988) reports for an annular container that a change in cell pattern is accompanied by an annihilation of corner cells, a fact also seen in figure 4. Typically this change is along an unstable branch.

The oscillatory flow found in Ahlers, Cannell & Steinberg (1985) near convection onset might be an example of a periodic flow caused by steady state/steady state interactions. Certainly, the transitions to time-periodic convection occurring at much larger Ma_0, such as found in Ciliberto, Simonelli & Arecchi (1986), are different to those described here. These are certainly more related to instabilities of boundary layers, such as described for porous media flows in Steen & Aidun (1988).

This work was partially supported by the US Army Research Office through the Mathematical Sciences Institute of Cornell University and partially supported by the National Aeronautical and Space Administration by grant NAG 3-801. The research was partially conducted using the Cornell National Supercomputer Facility, a resource of the Cornell Theory Center, which is funded in part by the National Science Foundation, New York State, the IBM Corporation and members of the Center's Corporate Research Institute. The work was finished at the Institute of Meteorology and Oceanography of the University of Utrecht, The Netherlands.

REFERENCES

Ahlers, G., Cannell, D. S. & Steinberg, V. 1985 Time dependence of flow patterns near the convective threshold in a cylindrical container. *Phys. Rev. Lett.* **54**, 1373–1375.

Bensimon, D. 1988 Pattern selection in thermal convection: experimental results in an annulus. *Phys. Rev.* A **37**, 200–206.

Berg, J. C. 1972 In *Recent Developments in Separation Science*, vol. 2, pp. 1–31. CRC.

BERGÉ, P. 1975 Rayleigh–Bénard instability: experimental findings obtained by light scattering and other optical methods. In *Fluctuations, Instabilities and Phase Transitions* (ed. T. Riste), pp. 323–352. Plenum.

BLOCK, M. J. 1956 *Nature* **178**, 650.

CHRISTODOULOU, K. N. & SCRIVEN, L. E. 1988 Finding leading modes of a viscous free surface flow: an asymmetric generalized eigenproblem. *J. Sci. Comput.* **3**, 355–405.

CILIBERTO, S., SIMONELLI, F. & ARECCHI, F. T. 1986 Measurement of temperature distribution in thermocapillary instability. *Il Nuovo Cimente* 7D, 195–202.

CLIFFE, K. A. 1983 Numerical calculations of two-cell and single-cell Taylor flows. *J. Fluid Mech.* **135**, 219–233.

CROSS, M. C., DANIELS, P. G., HOHENBERG, P. C. & SIGGIA, E. D. 1983 Phase winding solutions in a finite container above convective threshold. *J. Fluid Mech.* **127**, 155–183.

DAVIS, S. H. 1987 Thermocapillary instabilities. *Ann. Rev. Fluid Mech.* **19**, 403–435.

DIJKSTRA, H. A. 1988 Mass transfer induced convection near gas–liquid interfaces. PhD thesis, Department of Mathematics, University of Groningen, The Netherlands.

DIJKSTRA, H. A. & VAN DE VOOREN, A. I. 1989 Multiplicity and stability of steady solutions for Marangoni convection in a two-dimensional rectangular container with rigid sidewalls. *Numer. Heat Transfer* A **16**, 59–75.

DRAZIN, P. G. 1975 On the effects of sidewalls on Bénard convection. *Z. angew Math. Phys.* **26**, 239–243.

GUCKENHEIMER, J. & HOLMES, P. 1983 *Nonlinear Oscillations, Dynamical Systems and Bifurcations of Vector Fields.* Springer.

GOLDHIRSCH, I., ORSZAG, S. A. & MAULIK, B. K. 1987 An efficient method for computing leading eigenvalues and eigenvectors of large asymmetric matrices. *J. Sci. Comput.* **2**, 33–58.

GOLLUB, J. P. & BENSON, S. V. 1980 Many routes to turbulent convection. *J. Fluid Mech.* **100**, 449–470.

GOLUBITSKY, M. & SCHAEFFER, D. G. 1985 *Singularities and Groups in Bifurcation Theory*, part 1. Springer.

KELLER, H. B. 1977 Numerical solution of bifurcation and nonlinear eigenvalue problems. In *Applications of Bifurcation Theory* (ed. P. H. Rabinowitz). Academic.

KOSCHMIEDER, E. L. 1974 Bénard convection. *Adv. Chem. Phys.* **26**, 177–212.

KOSCHMIEDER, E. L. & PRAHL, S. A. 1990 Surface-tension-driven Bénard convection in small containers. *J. Fluid Mech.* **215**, 571–583.

METZENER, P. 1986 The effect of rigid sidewalls on nonlinear two-dimensional Bénard convection. *Phys. Fluids* **29**, 1373–1377.

MOORE, G. & SPENCE, A. 1980 The calculation of turning points of nonlinear equations. *SIAM J. Numer. Anal.* **17**, 567–576.

NIELD, D. A. 1964 Surface tension and buoyancy effects in cellular convection. *J. Fluid Mech.* **19**, 341–352.

PATBERG, W. B., KOERS, A., STEENGE, W. D. E. & DRINKENBURG, A. A. H. 1983 Effectiveness of mass transfer in a packed distillation column in relation to surface tension gradients. *Chem. Engng Sci.* **38**, 917–923.

PEARSON, J. R. A. 1958 On convection cells induced by surface tension. *J. Fluid Mech.* **4**, 489–500.

RILEY, D. S. & WINTERS, K. H. 1989 Modal exchange mechanisms in Lapwood convection. *J. Fluid Mech.* **204**, 325–358.

ROSENBLAT, S., HOMSY, G. M. & DAVIS, S. H. 1982 Nonlinear Marangoni convection in bounded layers. Part 2. Rectangular cylindrical containers. *J. Fluid Mech.* **120**, 123–138.

STEEN, P. H. & AIDUN, C. K. 1988 Time periodic convection in porous media: transition mechanism. *J. Fluid Mech.* **196**, 263–290.

STEWARD, W. J. & JENNINGS, A. 1981 A simultaneous iteration algorithm for real matrices. *ACM Trans. Math. Software* **7**, 184–198.

STORK, K. & MÜLLER, U. 1972 Convection in boxes: experiments. *J. Fluid Mech.* **54**, 599–611.

THOMSON, J. 1855 *Phil. Mag.* **10**, 330.

VAN DE VOOREN, A. I. & DIJKSTRA, H. A. 1989 A finite-element stability analysis of the

Marangoni problem in a two-dimensional container with rigid sidewalls. *Comput. Fluids* **17**, 467–485.

VIDAL, A. & ACRIVOS, A. 1966 Effect of nonlinear temperature profiles on the onset of convection driven by surface tension gradients. *I & EC Fundamentals* **7**, 53–58.

WERNER, B. & SPENCE, A. 1984 The computation of symmetry-breaking bifurcation points. *SIAM J. Numer. Anal.* **21**, 388–399.

WINTERS, K. H., PLESSER, TH. & CLIFFE, K. A. 1988 The onset of convection in a finite container due to surface tension and buoyancy. *Physica* D **29**, 387–401.

ZUIDERWEG, F. J. & HARMENS, A. 1958 The influence of surface phenomena on the performance of distillation columns. *Chem. Engng Sci.* **9**, 89–103.